Effect of air-sea-ice interaction on winter 1996 Southern Ocean subpolar storm distribution

Xiaojun Yuan, and Douglas G. Martinson
Lamont-Doherty Earth Observatory, Palisades, New York

W. Timothy Liu
Jet Propulsion Laboratory, Pasadena, California

Abstract, Air-sea-ice interaction processes in the Southern Ocean are investigated utilizing space-observed surface winds, sea ice concentration, and sea surface temperature (SST) from September through December, 1996. The sea ice edge (SIE) shows three ice-extent maxima around the Antarctic during September and October when sea ice coverage is maximum. They are located in the central Indian Ocean, east of the Ross Sea, and in the eastern Weddell Gyre. During September and October, most of the strong and long lasting storms initiate northeast of the three sea ice maxima. Such spatial distributions of storms and sea ice reflect coupling processes of the air-sea-ice interaction. A relatively stable, wave number 3 atmospheric circulation pattern that is believed to be fixed by the land-ocean distribution prevails during the ice maximum season. The ice-extent maxima coincide with strong southerlies and divergent wind fields associated with this pattern, which suggests that the mean atmospheric circulation determines the ice distribution. The ice-extent maxima can enhance the regional meridional surface pressure gradient and therefore strengthen the westerly winds north of the ice edge. The decreasing ice extent east of the ice maxima creates a local zonal thermal gradient which enhances local southerlies. This positive feedback between the wave pattern in the mean atmospheric circulation and ice distribution partially causes the eastward propagation of the ice maxima and also provides a favorable condition for cyclogenesis northeast of the ice-extent maxima. The mechanism of the cyclogenesis is the baroclinic instability caused by the cold air blown from the ice pack to the warm open-ocean waters. Where the SST is warmest off the SIE and the southerlies are the strongest, the potential for cyclogenesis is most likely. This is consistent with the observations.

1. Introduction

The air-sea-ice (ASI) system is complex and strongly coupled. In a marginal ice zone (MIZ), the transitional region between ice cover and open ocean, ASI interactions are particularly intense since the complex vertical interactions are further confounded by considerable lateral interactions between the open-ocean and ice-covered regions. These interactions are significant enough to influence even the large-scale atmospheric circulation and sea ice distribution. Indeed, numerous studies have examined the general relationship between the sea ice distribution and associated atmospheric circulation in the southern hemisphere [*Fletcher*, 1969; *Budd*, 1975; *Ackley and Keliher,* 1976; *Streten and Pike*, 1980; *Carleton*, 1981]. For example, *Ackley* [1981] reviewed previous work on sea ice and weather relationships, and pointed out that there is a broad zone of cyclogenesis associated with the entire pack ice/open-water region. The heat flux changes considerably in the area from continental ice to pack ice, resulting in strong baroclinicity that leads to the enhanced development of vortices. *Streten and Pike* [1980] showed that mean sea ice distribution was affected by the strength of the westerlies and the distribution of the Antarctic trough. *Cavalieri and Parkinson* [1981] found strong circumpolar flow near the ice edge during September, resulting in large changes in the ice edge associated with the circulation pattern, while weaker ice responses occur during the ice melt period. *Streten and Pike* [1980] and *Cavalieri and Parkinson* [1981] show that low-pressure centers usually occur east of the regions of rapid ice growth, where cold air advection predominates.

In addition to these large-scale influences and relationships, many of the ASI interactions suggest that the seaward side of the MIZ may favor storm generation. For example, numerous observational and modeling studies have shown that wind speeds increase significantly when crossing from an ice pack to open ocean [*Andreas et al*., 1984; *Chu*, 1986; *Guest et al*., 1995a, b]. Studies on mesoscale cyclogenesis suggest that baroclinic instability caused by strong horizontal thermal gradients, introduced by ice-ocean or land-ocean thermal contrast, is an important mechanism in the formation of polar storms in both northern [*Businger*, 1987; *Ese et al*., 1988] and southern [*Bromwich* 1989a, 1991; *Heinemann*, 1990; *Fitch and Carleton,* 1991] hemispheres. In addition, cold advection from ice pack to open ocean plays an important role in cyclogenesis, since the formation of a boundary layer baroclinic zone has been linked to such advection [*Turner and Row*, 1989]. Many theoretical studies have shown the importance of baroclinic instability as a primary mechanism in mesoscale cyclogenesis [*Mansfield*, 1974; *Okland,* 1987; *Moore and Peltier,* 1989; *Wiin-Nielsen*, 1989; *Emanuel and Rotunno*, 1989; *Graig and Cho,* 1989; *Fantini and Buzzi*, 1992]. Cyclogenesis is further enhanced by other mechanisms, such as air-sea interaction [*Emanuel and Rotunno,* 1989] or diabatic heating which reduces the static stability [*Graig and Cho*, 1989].

As processes associated with the air-sea-ice interaction and cyclogenesis in polar oceans have become better understood, in concert with modern satellite technologies providing global observations of sea ice, sea surface temperature (SST), and surface wind, we are now able to evaluate more completely the covarying spatial and temporal characteristics of the sea ice and surface wind fields. Furthermore, because of the relatively high spatial and temporal resolutions afforded by the satellite observations, we are able to more clearly put regional ASI relationships, such as those relating sea ice and polar cyclogenesis, into a global perspective. In this paper we take a step in that direction by examining the circumpolar relationship between the MIZ and cyclogenesis. The specific objectives of this study are to (1) characterize the spatial distribution of surface winds and storm systems as a function of sea ice distribution in the MIZ region of the subpolar Southern Ocean, and (2) use our current understanding of ASI interactions to deduce a mechanism explaining the observed relationships.

2. Data

The Defense Meteorological Satellite Program (DMSP) utilizing the Special Sensor Microwave/Imagers (SSM/I) provides continuous time series of brightness temperature in polar regions. Sea ice concentration data are derived from the SSM/I F13 daily brightness temperature using the NASA Team algorithm [*Gloersen and Cavalieri*, 1986; *Cavalieri et al.*, 1992]. For this study, we use these sea ice concentrations in 1996. The estimated accuracy of the derived sea ice concentration is 7% [*Gloersen et al.*, 1992]. Daily ice concentration data available in 25×25 km grids are digitized onto a 0.25° (latitude) and 1° (longitude) polar grid. We define the sea ice edge (SIE) as the equatormost position of the 30% isopleth of ice concentration. The SIE is not overly sensitive to the actual isopleth chosen to define it since the sea ice concentration increases rapidly near the ice edge during ice cover season. The choice of the 30% isopleth is to be consistent with a longer timescale study investigating global teleconnection between the sea ice edge position and extra-polar climate (X. Yuan and D. G. Martinson, Antarctic sea ice variability and its global connectivity, submitted to *Journal of Climate,* 1997).

The NASA scatterometer (NSCAT) is designed to acquire all-weather high-resolution measurements for deriving near-surface winds over the global oceans. A Japanese satellite, ADEOS, which carried the NSCAT instrument, was launched on August 16, 1996, with NSCAT measurements commencing in September 15, 1996. NSCAT scans two 600-km swaths on both sides. It provides wind speeds and directions over 90% of the ice-free global water surface in 2 days with a 25-km resolution within a swath. A recent study [*Bourassa et al.,* 1997] indicates that the rms difference between NSCAT-derived winds and high-quality ship observations is 1.6 m/s for wind speed and 13° for wind direction (given the wind speed range of 4-20 m/s). Surface winds are gridded by a successive corrections method [*Tang and Liu,* 1996] from NSCAT level 2 winds using selective directions. The wind stress is estimated as being proportional to the wind with a uniform constant of proportionality (W. Tang, personal communication, 1997). Available data in 1996 are twice-daily maps on a 0.25°×0.25° global grid from September 15 to December 31. To minimize the noise introduced by satellite sampling patterns, we apply a three-dimensional (3-D) smoother [*Zeng and Levy*, 1995] with a spatial scale of 900 km and a temporal scale of 5.5 days to the data and output the values on to a 1°×1° grid for the Southern Ocean from 30° to 75°S. Monthly means of τ_x and τ_y (zonal and meridional wind stress, respectively) are calculated from twice-daily maps; wind stress divergence is then calculated from the monthly mean τ_x and τ_y. Daily NSCAT level 3 winds (bin-averaged and gridded winds without interpolation between swaths) are also used in this study.

Weekly multichannel sea surface temperature (MCSST) data derived from the NOAA advanced very high resolution radiometer (AVHRR) for the period between September and December 1996 are on an equal-angle grid of 2048 columns by 1024 rows covering the entire globe. The weekly data are bin-averaged into a 1°×1° grid in the Southern Ocean from 30° to 75°S and then averaged in time to generate monthly mean SST fields. The magnitudes of sea surface temperature gradients, defined by

$$\sqrt{(\partial T / \partial x)^2 + (\partial T / \partial y)^2}\ ,$$

are then calculated from monthly mean fields.

3. Sea Ice Edge Distribution

Climatologically, the sea ice cover in September is at its winter maximum [*Zwally et al.*, 1983]. The monthly mean SIE for this period reveals three areas that have regionally maximum northern ice extent: the central Indian Ocean sector near 80°E, east of the Ross Sea near 215°E, and the Weddell Gyre near 360°E (Figure 1). For convenience, we designate these as the Indian Ocean, Ross Sea, and Weddell Sea ice maxima, respectively. The Weddell Sea ice maximum displays the most northern extent among the three, though the SIE anomaly (Figure 2) reveals that the Ross Sea ice maximum has the largest abnormal ice extent (more ice) relative to climatology around the Antarctic. The SIE in October retreats slightly while retaining spatial characteristics similar to those in September. The variability of SIE in September and October is small. The SIE retreats rapidly in November, but the spatial characteristics of the winter ice cover are still visible. Finally, in December the SIE loses its winter spatial characteristics due to the rapid spring decay. The largest regional ice melting indicated by the largest variability of the SIE occurs in the Weddell Gyre.

Figure 1

Figure 2

All three monthly mean ice-extent maxima propagate eastward from September to October but at different rates: The Indian Ocean maximum propagates at a mean speed of ~5.5 cm/s; the Ross Sea maximum propagates at ~15.7 cm/s, and the Weddell Sea maximum propagates at ~18.8 cm/s. Only the Ross Sea maximum continues to propagate eastward from October to November. The daily locations of these three sea ice maxima in September and October show details of such eastward propagation (Figure 3). Most apparent is that the Indian Ocean maximum propagates much slower than the other two ice maxima; the Weddell maximum does not propagate much during September but moves rapidly during October; and the Ross Sea maximum propagates more persistently during the 2 months but also shows an increasing propagation rate in October. The propagation speeds of the Weddell Sea and Ross Sea maxima are approximately double that of the Antarctic Circumpolar Wave [*White and Peterson*, 1996].

Figure 3

We consider September and October to be the seasons with maximum ice coverage and that November and December to represent the ice melt season. The main spatial characteristics of the SIE during the ice maximum season are the three ice-extent maxima. Such spatial characteristics can be clearly traced back in August (not shown here). Although the three ice-extent maxima propagate eastward slightly, their locations and shapes remain quite stable relative to the mean atmospheric circulation, which is presented in the next section. We believe that this SIE spatial distribution plays an important role in polar storm distribution, as will be seen next.

4. Surface Wind Distribution

To investigate large-scale air-sea-ice interactions, we concentrate on distributions of the monthly mean atmospheric circulation and severe weather systems as evidenced by the daily surface winds and stress, deduced from the NSCAT.

First, we examine the spatial distribution of strong storms. We concentrate predominantly on long-lasting severe weather systems instead of mesoscale cyclones, which only last for a day or so [*Carleton and Carpenter*, 1989, 1990]. In this study, we define a storm as any event displaying wind speeds of at least 14 m/s (equivalent to wind stress of 0.3 N/m^2) and lasting at least 3 days. The rotation of these storms will be examined by a rotary spectrum analysis (described below). There are 13 storms during the 47 days of the ice maximum season (from September 15 to October 31). Among them, only three start north of 55°S in the Antarctic Circumpolar Current (ACC) regions; they are located south of Australia and near the Drake Passage and usually last 3-6 days. The remaining 10 storms start near the SIE or MIZ south of 50°S, which is consistent with *Carleton* [1981], who found that cyclonic activity peaks in the 50°-75°S zone in September. These storms all initiate either north of the three ice-extent maxima or (in most cases) northeast of the maxima where the ice edge decreases eastward. They last 3-9 days. We call these storms marginal ice zone storms. Five of these "MIZ storms" initiate near the Ross Sea maximum, and then spin off into the ACC regions and influence a large area in the southeastern Pacific. These are usually the strongest storms and last 7 days on average. Three of the MIZ storms occur near the Indian Ocean maximum and influence areas in the eastern Indian Ocean and ACC regions south of Australia. They are moderate in strength and usually last about 5 days. The remaining two MIZ storms start east of the Weddell Sea maximum and influence smaller areas north of the SIE. They are relatively weak storms and last only 3-4 days. Plates 1 and 2 give examples of these storms, as indicated by the magnitude of wind stress.

Plate 1

Plate 2

Clearly, storms occur much less frequently as the sea ice begins to melt. In the 61 days of the ice melt season (November 1 to December 31), seven storms form. Five of them occur well north of the SIE in the ACC regions between 40° and 59°S. The duration of the storms varies from 3 days to 12 days. Of the remaining two, one starts east of the Ross Sea maximum in early November when the SIE still retains its winter spatial pattern; it lasts 7 days. Another storm occurs near the SIE in the Amundsen Sea, which is weak and only lasts 3 days.

To investigate the contribution of the sea ice distribution to cyclogenesis off the SIE, we use the daily surface winds at daily SIEs during the ice maximum season to examine the distribution of high wind occurrence. In general, there are stronger westerlies near the three ice maxima than in other locations around the Antarctic (Figure 4). Three reasons could explain such a distribution. First, ice-extent maxima are encroaching on the main jet of the westerlies, which is located about 50°S; Second, the polar lower surface pressure over the ice pack is moved northward by the maximum ice extent, resulting in a stronger geostrophic zonal wind: the westerlies. Third, frequent MIZ storms initialized north and northeast of the ice-extent maxima enhance the mean wind fields near ice maxima than in other locations. Strong southerlies, on the other hand, occur more frequently east of the three ice maxima where the SIE decreases eastward. The eastward decreasing SIE

Figure 4

provides a zonal thermal gradient which can geostrophically generate the southerlies in the areas.

To further understand cyclogenesis of the storms and their relationships with the ice cover, we would like to know the rotations of these systems. A rotary spectrum analysis is used here to show energy distributions of wind fields with different rotations. The rotary spectra are based on the decomposition of a velocity vector field:

$$\tau_x + i\tau_y = \sum_{\varpi} u(\varpi) e^{i\varpi t}$$

Thus counterclockwise (CCW) motions have negative frequency ($\varpi = -f$). Their energy is not the same as the energy of clockwise (CW) motions, which have positive frequency. In the southern hemisphere, a CW motion indicates a low-pressure system (cyclone) and a CCW motion presents a high-pressure system. The rotary spectrum analysis has been applied to many vector fields such as current meter data and wind fields [e.g., *Davis et al.,* 1981; *Yuan*, 1994]. For the NSCAT wind stress fields, the analysis shows that CW motions carry much more energy than CCW motions in a storm frequency band (periods of 5-10 days). The maximum energy of CW motions centers in the regions east of the Indian Ocean and Ross Sea ice maxima (Plate 3), where MIZ storms are frequently initiated.

Plate 3

Next we examine the general spatial patterns of the winds using monthly mean stress, τ_x, τ_y and stress divergence from September to December (Plates 4 and 5). The quasi-stationary waves apparent in the wind stress panels of the plates are characteristic of the southern hemisphere atmospheric circulation [*van Loon and Jenne*, 1972; *van Loon et al,* 1973; *Trenberth*, 1980; *Karoly,* 1985; *Quintanar and Mechoso,* 1995a,b]. The study of van Loon and Jenne (1972) showed that wave numbers 1 and 3 dominate, together accounting for 99% of the total variance in the annual mean 500-mbar pressure pattern. These waves are quite barotropic and extend from the surface to the lower stratosphere. The wave number 3 pattern is believed to be determined by the land-ocean distribution, accounting for its ridges near the three lower-latitude continents (Australia, southern Africa, and South America). It exists in all seasons. The wave number 1 was found to dominate in austral summer.

Plate 4

Plate 5

The NSCAT surface wind distribution clearly shows the wave number 3 pattern, specifically during September and October, 1996. In September, the zonal wind (as indicated by τ_x has three maxima around the Antarctic: northeast of the Indian Ocean ice-extent maximum; in the eastern Pacific east of the Ross Sea maximum, and in the Weddell Gyre west of the Weddell Sea maximum. Corresponding to these zonal wind maxima, there are three southerly maxima separated by three northerly maxima around the entire Southern Ocean defining a wave number 3 atmospheric circulation pattern which is spatially consistent with the wave number 3 pattern found by *van Loon and Jenne* [1972]. Maximum southerlies occur east of the Indian Ocean and Ross Sea maxima, where the MIZ storms are frequently initiated. The divergence of the wind stress is rather noisy, but strongly divergent patterns are evident near the Indian Ocean and Ross Sea ice maxima, a convergent wind field is evident near the Weddell Sea ice maximum.

The October mean circulation pattern does not change significantly relative to that in September, except in the Weddell Gyre, where the zonal wind maximum shifts from west to east of the Weddell Sea ice maximum and the mean southerlies disappear. The wave number 3 pattern still exists, with a weaker branch in the Weddell Gyre. The wind field is still divergent near the Indian Ocean and Ross Sea maxima while weakly divergent near the Weddell Sea maximum. The divergent winds near or east of the ice maxima are expected theoretically. A thermal gradient exists across the ice edge. Air is blown from the ice pack to the open ocean perpendicular to the SIE due to this thermal gradient and then turns left because of the Coriolis force. Near a SIE maximum, it results in strong northerlies and weak easterlies on the western edge of the maximum; strong easterlies at the ice maximum; and weak easterlies and strong southerlies on the eastern edge. This leads to (1) wind convergence (divergence) west (east) of the ice maximum, and (2) weak (strong) southerlies west (east) of the maximum. The coexistence of the ice-extent maxima and southerlies as well as the maximum wind stress divergence during the maximum ice season suggest an interaction between the mean atmospheric circulation and the sea ice maxima.

As the ice rapidly disintegrates in November and December, the wave number 3 pattern is lost in the mean surface wind stress fields because of the seasonally strengthened wave number 1 component. November winds display strong westerlies over the ACC region, with a maximum in the eastern Pacific and some easterlies in the eastern Pacific, while southerlies still exist near the Indian Ocean and Ross Sea maxima. December zonal winds are more evenly distributed around the Antarctic, with a maximum centered in the ACC regions. The meridional wind is much weaker then.

5. Sea Surface Temperature Distribution

When cold air is blown off ice packs over the open ocean, it becomes unstable while gaining energy from the positive heat flux associated with the warmer ocean. Consequently, the sea surface temperature north of the SIE will determine to some extent the horizontal and vertical atmospheric thermal gradients in the MIZ. Therefore the distribution of SST north of the SIE likely plays a role in the MIZ cyclogenesis.

Spatial distributions of the monthly mean SST north of the SIE in September and October show that SSTs are warmest in the regions west of the Ross Sea around 180°E, east of the Ross Sea around 220°E, and in the eastern Pacific near 280°E (Figure 5). The SST meridional gradients in these three regions are also relatively strong. However, among these three regions, only the one east of the Ross Sea coincides with prevailing southerlies and therefore has the right atmospheric condition for cyclogenesis (see discussion in section 6). The northerlies bring warm air from the ocean over the ice pack in the other two regions, which can cause cyclogenesis over the ice pack but do not contribute to the cyclogenesis north of the SIE [*Carrasco and Bromwich*, 1993; *Guest et al.*, 1995b]. The SST north of the SIE near the Indian Ocean ice maximum is 2°-

Figure 5

4°C cooler than that near the Ross Sea ice maximum, and its gradient is moderate. However, southerly winds prevail there, which make it a favorite location for storms (discussed in section 6). Certainly, the difference of 2°-4°C between the Indian Ocean and east Pacific is a small adjustment to the already large temperature contrast when cold air is blown over the warm ocean. However, this small adjustment may play a role in cyclogenesis and particularly when the relative phasing between SST and winds, following the SIE, are favorable, as is truly the case for the Ross Sea and Indian Ocean ice maxima positions.

As the SIE retreats southward during ice melting season, especially in December, the gradients of SST north of the SIE become weaker. The thermal gradient of surface air across the SIE is much weaker than that in the ice maximum season.

6. Air-Sea-Ice Interaction and Cyclogenesis

The sea ice and surface wind patterns suggest the possibility of a coupling during the latter part of the austral winter in 1996. Here we discuss potential coupling mechanisms.

6.1 Mean Atmospheric Circulation and Ice Distribution

As shown earlier, the spatial characteristics of the SIE with its three ice-extent maxima do not change significantly relative to the atmospheric circulation during the ice maximum season. Meanwhile, a relatively stable, wave number 3 atmospheric circulation prevails in the Southern Ocean. This ice distribution and atmospheric circulation pattern is established by August (which can be found in other wind products, such as National Center for Environmental Predication (NCEP) surface winds and ERS-2 winds). The ice-extent maxima, in the Indian Ocean and east of the Ross Sea, coincide with strong southerlies and divergent wind fields. This is consistent with a persistent geographically-constrained mean atmospheric circulation pattern creating the ice extent maxima in regions where southerlies prevail and the wind field is divergent. The ice-extent maxima can be generated by two processes: ice advance directly due to advection by winds and ice formation due to intense cooling when cold air is blown from the ice pack [*Massom*, 1992]. A similar influence of the standing atmospheric circulation on sea ice distribution was found in the northern hemisphere [*Cavalieri and Parkinson*, 1987]. The Weddell Sea maximum is broader than the other two maxima. The wind field is more variable near this maximum, especially with its weaker branch of the wave number 3 pattern and variable meridional winds in October. However, we cannot exclude the possibility that the mean atmospheric circulation influences the formation of this ice maximum in September or even in August. Also, frequent southerlies east of the Antarctic Peninsula, so-called barrier winds, advect large quantities of ice northward [*Schwerdtfeger,* 1975, 1979]. The barrier winds are generated when the prevailing easterlies over the central and southern Weddell Sea are blocked by the Peninsula mountains. On the other hand, the (seafloor) topographically guided path of the ACC, which sets the position of the polar front, could also play a role in shaping the SIE around the Antarctic. The southern boundary of the ACC [*Orsi et al.,* 1995] indicates such a possibility, as seen in Figure 6.

Figure 6

Once an ice-extent maximum is formed, it can potentially enhance the meridional surface pressure gradient and therefore strengthen the westerlies north of the ice maximum. This is because the position of the polar front is relatively stable, and this front fixes the general pressure meridional gradient; thus, as the ice impinges upon the front, the lower polar pressure moves northward and its meridional gradient is compressed. The decreasing ice extent east of the ice maximum can create a zonal thermal gradient which enhances local southerlies through geostrophic adjustment. For the same reason, any southerlies west of the ice maximum will be weakened because of the westward decreasing ice edge. Figure 6 shows the thermal winds due to the ice distribution. A close look at Figure 4 and Plate 4 does find that southerlies are much stronger east of the ice maxima than west of the ice maxima except in the Weddell Gyre. This local positive feedback from the ice distribution enforces the atmospheric wave pattern in the lower boundary layer or at least helps to maintain the wave pattern against dissipation.

6.2. Propagation of Ice Maxima

The coupling process between the wave pattern in the mean atmospheric circulation and ice distribution would also contribute to the observed eastward propagation of the ice maximum. The eastward propagating speed of the ice maxima can be attributed to three factors: direct advection due to the zonal wind and ACC; phase propagation due to the coupling process between the ice distribution and atmospheric wave pattern as mentioned above; and thermodynamic ice growth and melt.

An ice floe can be advected by an ocean current and the surface wind. The surface wind usually dominates the advection [*Massom*, 1992]. *Martinson and Wamser* [1990] showed that sea ice in the divergent Antarctic polar seas moves at ~3% of the wind speed at 20° to the left of the wind in addition to the advection with the mean ocean current. The mean ocean current in this region is that of the southern arm of the ACC, moving at a speed less than the mean core speed of about 11 cm/s [*Whitworth and Peterson*, 1985]. Both the zonal wind and ACC advect the ice maxima eastward.

The stronger southerlies east of the ice maxima will advect local sea ice northward and also encourage ice growth by providing strong surface cooling. On the other hand, weaker southerlies west of the ice maxima will limit northward ice advance. As a result, the ice maxima will expand eastward. This phase shifting effect should be related to the spatially decreasing SIE slope east of the maxima (Figure 7), though the very small sample size (3) precludes an evaluation of the significance of this relationship. Both the Ross Sea and Weddell Sea maxima have steep eastward decreasing slopes, while the Indian Ocean maximum has a much milder slope. The steepness of the ice edge retreating east of the ice maximum determines the strength of the zonal thermal gradient and therefore the strength of the meridional geostrophic adjustment. This can be one reason that the Indian Ocean

Figure 7

maximum propagates much slower than the other two ice maxima. Moreover, the propagation of the Weddell Sea maximum gives an example of the importance of the phase shifting due to the positive coupling process. During September, the southerlies prevail west of the Weddell Sea ice maximum (Plate 4). The geostrophic wind introduced by the ice distribution works against the mean circulation. No clear propagation of the ice maximum is found (Figure 3). However, the southerlies prevail east of the ice maximum during October. The positive feedback kicks in, and the ice maximum propagates quickly.

In addition to the thermodynamic process involved in the phase propagation of the ice maxima, another thermodynamic process needs to be considered. When an ice floe is advected eastward and meets warmer seawater, it can be melted. This process works against the eastward propagation of the ice maxima. The net propagation rate of the ice maxima are the balance of above processes. With the current data sets, we are unable to quantitatively, or even qualitatively, separate the contributions from these processes.

6.3. Cyclogenesis, Sea Ice, and SST

Fitch and Carleton (1991) found that the outbreak of storms in the Antarctic between 110°E and 120°W is concentrated in the Ross Sea region. They suggested that a strong horizontal thermal gradient in the lower troposphere such as that present across the MIZ is an important factor for the formation of mesoscale vortices, but not the only one: Cold advection from the ice pack to open ocean was also important. Similar results were found in the Weddell Sea region [*Heinemann*, 1990] and in the northern hemisphere [*Businger, 1987; Ese et al.*, 1988]. As a special case, katabatic winds are candidates for such a cold advection off the Antarctic continent [*Bromwich*, 1986, 1989b; *Parish and Bromwich,* 1989; *Fitch and Carleton*, 1991; *Carrasco and Bromwich,* 1993; *Carleton and Fitch*, 1993]. Even though we are examining larger and more severe systems than mesoscale cyclones, the above mechanisms for cyclogenesis seem to apply in this case as well. On the circumpolar scale, we suggest that the semistationary planetary wave pattern, large-scale sea ice distribution, and SST north of the sea ice edge all contribute to the formation of severe storms. Specifically, the positive feedback of the sea ice distribution to the mean atmospheric circulation described above not only strengthens the atmospheric wave pattern but also provides a favorable condition for cyclogenesis in the open ocean northeast of the ice-extent maxima. As observed, all MIZ storms initiate in the areas north or northeast of the ice maxima during the ice maximum season. When southerlies near the ice maxima blow cold air off the ice pack over warm open-ocean waters, a baroclinic instability is generated, which is the primary mechanism of cyclogenesis near the MIZ [*Fitch and Carleton*, 1991; *Heinemann,* 1990; *Guest et al.,* 1995b]. This mechanism is consistent with the storms off the three ice maxima. Moreover, the positive feedback from ice to atmosphere generates stronger southerlies east of the ice maxima and stronger westerlies north of the maxima, which provide momentum to spin off cyclones in these regions.

In the region east of the Ross Sea, southerlies blow cold air from the ice pack to open ocean. The SIE decreases eastward, generating a zonal thermal gradient which geostrophically enhances the local southerly. Both the ice distribution and atmospheric circulation provide a baroclinicity seaward of the SIE which is favorable to cyclogenesis. In addition to these cryosphere and atmosphere conditions, the SST north of the SIE is warmer and the meridional gradient of the SST is stronger here than in most regions around the Antarctic. When the cold air is blown over this warmer ocean, it is more susceptible to baroclinic instability. The coincidence of warmer SST, higher meridional SST gradient, sea ice extent maximum, and prevailing southerlies in the region east of the Ross Sea certainly provides an ideal condition for cyclogenesis north of the SIE. Indeed, the region east of the Ross Sea is the prime location for storms during the maximum ice season in 1996. The storms in this region not only occur more frequently, but also last longer (7 days, on average) and influence a larger area than the storms found in other regions.

The atmospheric circulation pattern and the sea ice distribution in the Indian Ocean are similar to those in the region east of the Ross Sea. However, the SST north of the Indian Ocean ice maximum is about 2°-4°C colder than that in the region east of the Ross Sea. This is still a favorable location for generating storms due to the ice distribution and atmospheric circulation. The storms found in this region are less frequent, weaker and influence a smaller area than the storms east of the Ross Sea. This may reflect the weaker SST and the reduced atmospheric circulation-ice feedback associated with a weaker ice maximum.

The weakest storms are found in the region east of the Weddell Sea ice maximum. Here only two storms were initiated east of the Weddell Sea . They occurred during October 8-10 and October 18-20, when southerlies prevailed locally. Although the Weddell Gyre has the most northern ice extent among the three ice maxima, the variable meridional winds (infrequent southerlies) and colder SST north of the SIE make it a less favorable location for cyclogenesis compared with the other two regions.

As the SIE retreats during the ice-melting season (November and December), the winter spatial characteristics of the SIE gradually disappear. The SST north of the SIE, which is now displaced southward into the colder polar gyre waters, becomes colder and the SST gradient becomes weaker, which reduces the air temperature contrast across the SIE. The atmospheric wave number 3 pattern is masked because of a stronger wave number 1 pattern. As the conditions favorable to cyclogenesis disappear, the storms occur less frequently and are often initiated anywhere over the Antarctic Circumpolar Current region well north of the MIZ rather than near the SIE and in specific locations. *Cavalieri and Parkinson* [1981] also found the atmospheric circulation and ice field to be decoupled during the ice melting season.

7. Discussion and Conclusions

Frequent storms in an area can precondition the structure of the water column for future air-sea-ice interaction. For example, if storms form in particular regions of polar waters, they can dome the pycnocline and sharpen it, making conditions favorable for transporting heat from the ocean to the atmosphere, deep convection, and a weak ice cover [*Martinson,* 1990]. On longer timescales, the surface stress over the ACC dictates the depth to which deep isopycnals are elevated in the polar gyres, making them more susceptible to ventilation. Therefore understanding the relationship between the ice distribution and the atmosphere, particularly the storm distribution and the mechanisms that cause this distribution, is important in understanding local, regional, and global implications of the air-sea-ice interaction.

We have presented satellite observations of the atmosphere, ocean, and cryosphere around the Antarctic during September to December, 1996. This study shows a coupled system involved with a standing wave number 3 phenomenon in the atmosphere and cryosphere of the Southern Ocean. This coupled system has synoptic-to-seasonal timescales. It is different from the propagating wave number 2 phenomenon found by *White and Peterson* [1996], which is reflected in interannual timescales. However, *Raphael et al.* [1997] found that the atmospheric quasi-stationary waves are influenced by El Niño-Southern Oscillation (ENSO) events. Therefore, there is a possibility that these two coupled systems are related or interact. This warrants further study. In addition, the southern boundary of the ACC also has a wave number 3 pattern [*Orsi et al.*, 1995] possibly constrained by seafloor topography. Further studies are needed to elucidate the relationship between this oceanic wave pattern and the wave pattern in the atmosphere-cryosphere coupled system.

The ADEOS satellite carrying the NSCAT instrument failed in June 1997, and therefore only one winter-to-spring season is analyzed in this study. Consequently, the small sample size limits our ability to draw statistically rigorous conclusions. Regardless, this analysis suggests the following:

1. The spatial characteristics of the sea ice distribution during September and October, 1996 are dominated by three ice-extent maxima in the Central Indian Ocean, east of the Ross Sea and in the eastern Weddell Gyre. This spatial characteristic of the sea ice edge (SIE) does not change significantly during the ice maximum season, although the maxima do propagate eastward slightly at speeds of 0.05-0.18 m/s.

2. The mean atmospheric circulation shows a semistationary (nonpropagating) wave number 3 pattern during the ice maximum season. The ice-extent maxima coincide with the strong southerly branches of this pattern and divergent wind fields. The atmospheric pattern is thought to be fixed by the southern hemisphere land-ocean distribution, which suggests that the mean atmospheric circulation dominates the ice distribution, although we cannot rule out the topographically guided ACC as playing a major influence.

3. The ice maxima enhance meridional pressure gradients to the north and zonal thermal gradients to the east, therefore enhancing westerlies north of the maxima and southerlies east of the maxima through geostrophic adjustments. The enhanced westerlies reflect an increase in the existing regional meridional pressure gradient, whereas the enhanced southerlies

reflect the development of a local zonal pressure gradient as function of ice-ocean temperature contrast. These serve as a positive feedback between the wave pattern in the mean atmospheric circulation and ice distribution. The stronger southerlies east of the ice maxima provide strong baroclinity in the open ocean north of the SIE, which is favorable for cyclogenesis. The strength of the geostrophic southerlies is determined by the decreasing slope of the SIE east of the ice maxima. Where the SIE decreasing slope is large, the southerlies are the strongest and the SST off the SIE is the warmest, and thus the potential for cyclogenesis is highest. This is consistent with the observations.

4. Most severe storms in the subpolar Southern Ocean are initiated northeast of the three ice maxima during the ice maximum season and are spun off into ACC regions. Northeast of the Ross Sea ice maximum is the region showing the highest frequency of strong and long-lasting storms due to most favorable cyclogenetic conditions in the air-sea-ice system.

5. The sea ice maxima propagate eastward during the ice maximum season. The propagation can be caused by direct advection of the zonal wind and the ACC; thermodynamic growth/melt processes; and a phase shift due to a positive feedback between ice distribution and the atmospheric circulation — stronger (weaker) southerlies east (west) of ice maxima. The latter is apparently related to the decreasing ice edge slope east of the maxima, which determines the strength of the zonal thermal gradient introduced by the sea ice distribution.

6. Relatively high SST and strong meridional SST gradients north of the ice maxima further enhance the chance of cyclogenesis through stronger heat fluxes. The stronger and more frequent storms initiated northeast of the Ross Sea ice maximum provide such an example. In this region, not only do the atmospheric circulation and sea ice distribution strongly favor cyclogenesis, but also the SST north of the SIE is 2°-4°C higher than the SST north of the other two ice maxima.

7. The atmospheric wave number 3 pattern becomes masked during November and December as the wave number 1 pattern begins to dominate. The SIE retreats quickly during the same period, and the winter spatial characteristics of the SIE gradually disappear. The SST north of the SIE becomes colder. Storms occur less frequently and are typically initiated over the Antarctic Circumpolar Current regions to the north of the retreating SIE and do not concentrate in specific zonal locations.

Acknowledgments, The authors thank Wenqing Tang for providing gridded NSCAT surface wind stress data. Discussions with Ralph Milliff were very helpful. X. Yuan was supported by NASA grant JPLCIT-960868, D. G. Martinson was supported by Ford Motor Company Environmental Research grant 44024, and W. T. Liu was supported by the NASA Scatterometer Project at JPL. Lamont-Doherty Earth Observatory contribution number 5855.

References

Ackley, S. F., A review of sea-ice weather relationships in the southern hemisphere, in *Proceedings of the 17th General Assembly of IUGG on Sea Level, Ice and Climatic change*, edited by I. Allison, *IAHS*, Publ., *131*, 127-159, 1981.

Ackley, S. F. and T. E. Keliher, Antarctic sea ice dynamics and its possible climatic effects, *Arctic Ice Dyn. Joint Exp. Bull.*, *33*, 53-56, 1976.

Andreas, E. L., W. B. Tucker III, and S.F. Ackly, Atmospheric boundary-layer modification, drag coefficient, and surface heat flux in the Antarctic marginal ice zone, *J. of Geophys. Res., 89,* 649-661, 1984.

Bourassa, M. A., M. H. Freilich, D. M. Legler, W. T. Liu and J. J O'Brien, Wind observations from new satellite and research vessels agree, *EoS*, *Trans. AGU*, *78*. (51), 597, 1997.

Bromwich, D. H., Boundary layer meteorology of the western Ross Sea, *Antarct. J. U. S.*, *21*(5), 235-237, 1986.

Bromwich, D. H., Subsynoptic-scale cyclone developments in the Ross Sea sector of the Antarctic, in *Polar and Arctic Lows*, edited by P.F. Twitchell, E. A. Rasmusssen, and K. L. Davidson, pp. 331-345, A. Deepak, Hampton, Va., 1989a.

Bromwich, D. H., An extraordinary katabatic wind regime at Terra Nova Bay, Antarctica, *Mon. Weather Rev., 117,* 688-695, 1989b.

Bromwich, D. H., Mesoscale cyclogenesis over the southwestern Ross Sea linked to strong katabatic winds, *Mon. Weather Rev*., *119*, 1736-1752, 1991.

Budd, W. F., Antarctic sea-ice variations from satellite sensing in relation to climate, *J. Glaciol*., *15*, 417-427, 1975.

Businger, S., The synoptic climatology of polar-low outbreaks over the Gulf of Alaska and the Bering Sea, Tellus, Ser. A. 39, 307-325, 1987.

Carleton, A. M., Monthly variability of satellite-derived cyclonic activity for the southern hemisphere winter, *J. Climatol*., *1*, 21-38, 1981.

Carleton, A. M., and D. A. Carpenter, Intermediate-scale sea ice atmosphere interactions over high southern latitudes in winter, *GeoJournal*, *18,* 87-101, 1989.

Carleton, A. M., and D. A. Carpenter, Satellite climatology of "polar lows" and broadscale climatic associations for the southern hemisphere, *Int. J. Climatol*., *10*, 219-246, 1990.

Carleton, A. M., and M. Fitch, Synoptic aspects of Antarctic mesocyclones, *J. Geophys. Res., 98,* 12,997-13,018, 1993.

Carrasco, J. F. And D. H. Bromwich, Mesoscale cyclogenesis dynamics over the Southwestern Ross Sea, Antarctica, *J. Geophys. Res., 98,* 12,973-12,995, 1993.

Cavalieri, D. J., The validation of geophysical products using multisensor data, in *Microwave Remote Sensing of Ssea Ice*. Geophys. Monogr. Ser., vol. 68, edited by F. Carsey, pp 233-242, AGU, Washington, D. C., 1992.

Cavalieri, D. J., and C. L. Parkinson, Large-scale variations in observed Antarctic sea ice extent and associated atmospheric circulation, *Mon. Weather Rev*., *109*, 2323-2336, 1981.

Cavalieri, D. J., and C. L. Parkinson, On the relationship between atmospheric circulation and the fluctuations in the sea ice extents of the Bering and Okhotska Seas, *J. Geophys. Res., 92*, 7141-7162, 1987.

Cavalieri, D. J., J. et al., NASA sea ice validation program for the DMSP SSM/I: Final report, *NASA Tech. Memo. 104559*, 126 pp., 1992.

Chu, P. C., An ice/air feedback mechanism for the migration of the marginal ice zone, *Marginal Ice Zone Exp Bull VII,* 54-64, March 1986.

Davis, R. E., R. deSzoeke, D. Halpern, and P. P. Niiler, Variability in the upper ocean during MILE, Part I: The heat and momentum balances, *Deep-Sea Res.,* part A, *28*, 1427-1451, 1981.

Emanuel, K. A., and R. Rotunno, Polar lows as arctic hurricanes, *Tellus* , *Ser. A, 41*, 1-17, 1989.

Ese, T., I. Kanestrom, and K. Pedersen, Climatology of polar lows over the Norwegian and Barents seas, *Tellus, Ser. A, 40,* 248-255, 1988.

Fantini, M., and A. Buzzi, Numerical experiments on a possible mechanism of cyclogenesis over the circum-antarctic ocean, in *Conference Proceedings, Third Workshop, Italian Research on*

Antarctic Atmosphere, vol. 34, edited by M. Colacino, G. Giovanelli, and L. Stefanutti, pp. 79-89, Ital. Phys. Soc., Bologna, Italy, 1992.

Fitch, M., and A. M. Carleton, Antarctic mesocyclone regimes from satellite and conventional data, *Tellus Ser. A, 44*, 180-196, 1991.

Fletcher, J. O, Ice extent on the southern ocean and its relation to world climate, Rep. RM-5793-NSF, 108 pp., Rand Corp., Santa Monica, California, 1969.

Gloersen, P., and D. J. Cavalieri, Reduction of weather effects in the calculation of sea ice concentration from microwave radiances, *J. Geophys. Res., 91*, 3913-3919, 1986.

Gloersen, P., W. J. Campbell, D. J. Cavalieri, J. C. Comiso, C. L. Parkinson, and H. J. Zwally, Arctic and Antarctic sea ice, 1978-1987: Satellite passive-microwave observations and analysis, *NASA Spec. Publ. SP-511*, 290 pp., 1992.

Graig, G., and H.-R. Cho, Baroclinic instability and CISK as the driving mechanisms for polar lows and comma clouds, in *Polar and Arctic Lows*, edited by P.F. Twitchell, E. A. Rasmusssen, and K. L. Davidson, pp. 131-140, A. Deepak, Hampton, Va., 1989.

Guest, P. S., J. W. Glendening, and K. L. Davidson, An observational and numerical study of wind stress variations within marginal ice zones, *J. of Geophys. Res.*, *100*, 10,887-10,904, 1995a.

Guest, P. S., K. L. Davidson, J. E. Overland, and P. A. Frederickson, Atmosphere-ocean interactions in the marginal ice zones of the Nordic Seas, in Arctic Oceanography: *Marginal Ice Zone and Continental Shelves, Coastal and Estuarine Studies,* Vol. 49, edited by W. O. Smith Jr. And J. M. Grebmeier, pp. 51-95, AGU, Washington D. C., 1995b.

Heinemann, G., Mesoscale vortices in the Weddell Sea region (Antarctica), *Mon. Weather Rev.*, *118,* 779-793, 1990.

Karoly, D. J., An atmospheric climatology of the southern hemisphere based on ten years of daily numerical analyses (1972-82), Part II: Standing wave climatology, *Aust. Meteorol. Mag.*, *33*, 105-116, 1985.

Mansfield, D. A., Polar lows: The development of baroclinic disturbances in cold air outbreaks, *Q. J. R. Meteorol. Soc.*, *100*, 541-554, 1974.

Martinson, D. G., Evolution of the Southern Ocean winter mixed layer and sea ice: Open ocean deep water formation and ventilation, *J. of Geophysical Research*, 95, 11641-11654, 1990.

Martinson, D. G., and C. Wamser, Ice drift and momentum exchange in winter Antarctic pack-ice, *J. Geophys. Res., 95*, 1741-1755, 1990.

Massom, R. A., Observing the advection of sea ice in the Weddell Sea using buoy and satellite passive microwave data, *J. Geophys. Res.*, *97*, 15,559-15,572, 1992.

Moore, K. G. W., and W. R. Peltier, On the development of polar low wavetrains, in *Polar and Arctic Lows*, edited by P.F. Twitchell, E. A. Rasmusssen, and K. L. Davidson, pp. 141-153, A. Deepak, Hampton, Va., 1989.

Okland, H., Heating by organized convection as a source of polar low intensification, *Tellus, Ser. A, 39,* 397-407, 1987.

Orsi, A. H., T. Whitworth III, and W. D. Nowlin Jr., On the meridional extent and fronts of the Antarctic Circumpolar Current, *Deep-Sea Res.,. 42,* 641-673, 1995.

Parish, T. R., and D. H. Bromwich, Instrumented aircraft observations of the katabatic wind regime near Terra Nova Bay, *Mon. Weather Rev.*, *117*, 1570-1585, 1989.

Qiu, B., and F.-F. Jin, Antarctic circumpolar waves: An indication of ocean-atmosphere coupling in the extratropics, *Geophys. Res. Lett., 24*(21), 2585-2588, 1997.

Quintanar, A. I., and C. R. Mechoso, Quasi-stationary waves in the southern hemisphere, 1, Observational data, *J. Clim.*, *8* (11), 2659-2672, 1995a.

Quintanar, A. I., and C. R. Mechoso, Quasi-stationary waves in the southern hemisphere, 2. Generation mechanisms, *J. Clim.*, *8* (11), 2673-2690, 1995b.

Raphael, M., R. F. Milliff, T. J. Hoar, and H. Van Loon, Quasi-stationary wave variabilities at the surface and at 500 hPa from NSCAT, ERS, and NCEP, in *Proceedings of the NASA Scatterometer Science Symposium,* pp. 126-129, 1997.

Schwerdtfeger, W., The effect of the Antarctic Peninsula on the temperature regime of the Weddell Sea, *Mon. Weather Rev.*, *103*, 45-51, 1975.

Schwerdtfeger, W., Meteorological aspects of the drift of ice from the Weddell Sea toward the mid-latitude westerlies. *J. Geophys. Res., 84*, 6321-6328, 1979.

Streten, N. A., and D. J. Pike, Characteristics of the broadscale Antarctic sea ice extent and the associated atmospheric circulation 1972-1977, *Arch. Meteorol. Geophys. Bioklim*atol., *Ser. A. 29*, 279-299, 1980.

Tang, W., and W. T. Liu, Objective interpolation of scatterometer winds, *JPL Publ. 96-19*, 16 pp., 1996.

Trenberth, K. E., Planetary waves at 500 mb in the southern hemisphere, *Mon. Weather Rev., 108*, 1378-1389, 1980.

Turner, J., and M. Row, Mesoscale vortices in the British Antarctic territory, in *Polar and Arctic Lows*, edited by P.F. Twitchell, E. A. Rasmusssen, and K. L. Davidson, pp. 347-356, A. Deepak, Hampton, Va., 1989.

van Loon, H., and R. L. Jenne, The zonal harmonic standing waves in the southern hemisphere, *J. Geophys. Res., 77*, 992-1003, 1972.

van Loon, H., R. L. Jenne, and K. Labitzke, Zonal harmonic standing waves, *J.Geophys. Res., 78*, 4463-4471, 1973.

White, B. W., and R. G. Peterson, An Antarctic circumpolar wave in surface pressure, wind, temperature and sea ice extent, *Nature*,. *380*, 699-702, 1996.

Whitworth, T. III and R. G. Peterson, Volume transport of the Antarctic Circumpolar Current from bottom pressure measurements, *J. Phys. Oceanogr., 15*, 810-816, 1985.

Wiin-Nielsen, A., On the precursors of polar lows, in *Polar and Arctic Lows*, edited by P.F. Twitchell, E. A. Rasmusssen, and K. L. Davidson, pp. 85-107, A. Deepak, Hampton, Va., 1989.

Yuan, X., Characteristics and frontogenesis of the subarctic front in the North Pacific, Ph.D. thesis, Scripps Inst. of Oceanogr., Univ. of Calif., San Diego, 1994.

Zeng, L., and G. Levy, Space and time aliasing structure in monthly mean polar-orbiting satellite data, *J. Geophys. Res., 100*, 5133-5142, 1995.

Zwally, H. J., J. C. Comiso, C. L. Parkinson, W. J. Campbell, F. D. Carsey, and P. Gloersen, Antarctic Sea Ice, 1973-1976: Satellite Passive-Microwave Observations, Sci. and Tech. Inf. Branch, Nat. Aeronaut. and Space Admin., Washington, DC, 206pp., 1983.

W. T. Liu, Jet Propulsion Laboratory 300-323, Pasadena, CA 91109 (email: liu@pacific.jpl.nasa.gov.)

D. G Martinson and X. Yuan, Lamont-Doherty Earth Observatory of Columbia University, Palisades, NY 10964. (Email: dgm@ldeo.columbia.edu; xyuan@ldeo.columbia.edu.)

(Received April 18, 1998; revised August 10, 1998;
accepted August 17, 1998.)

Paper number 98JD02719.
0148-0227/98/98JD-02719$09.00

Running Heads

YUAN ET AL.: AIR-SEA-ICE INTERACTION AND STORM DISTRIBUTION

YUAN ET AL.: AIR-SEA-ICE INTERACTION AND STORM DISTRIBUTION

YUAN ET AL.: AIR-SEA-ICE INTERACTION AND STORM DISTRIBUTION

YUAN ET AL.: AIR-SEA-ICE INTERACTION AND STORM DISTRIBUTION

YUAN ET AL.: AIR-SEA-ICE INTERACTION AND STORM DISTRIBUTION

YUAN ET AL.: AIR-SEA-ICE INTERACTION AND STORM DISTRIBUTION

YUAN ET AL.: AIR-SEA-ICE INTERACTION AND STORM DISTRIBUTION

YUAN ET AL.: AIR-SEA-ICE INTERACTION AND STORM DISTRIBUTION

YUAN ET AL.: AIR-SEA-ICE INTERACTION AND STORM DISTRIBUTION

YUAN ET AL.: AIR-SEA-ICE INTERACTION AND STORM DISTRIBUTION

YUAN ET AL.: AIR-SEA-ICE INTERACTION AND STORM DISTRIBUTION

YUAN ET AL.: AIR-SEA-ICE INTERACTION AND STORM DISTRIBUTION

YUAN ET AL.: AIR-SEA-ICE INTERACTION AND STORM DISTRIBUTION

YUAN ET AL.: AIR-SEA-ICE INTERACTION AND STORM DISTRIBUTION

YUAN ET AL.: AIR-SEA-ICE INTERACTION AND STORM DISTRIBUTION

YUAN ET AL.: AIR-SEA-ICE INTERACTION AND STORM DISTRIBUTION

YUAN ET AL.: AIR-SEA-ICE INTERACTION AND STORM DISTRIBUTION

YUAN ET AL.: AIR-SEA-ICE INTERACTION AND STORM DISTRIBUTION

YUAN ET AL.: AIR-SEA-ICE INTERACTION AND STORM DISTRIBUTION

Figure Captions

Figure 1. The mean Antarctic sea ice edge (solid lines) derived from Special Sensor Microwave Imager ice concentration data for September, October, November, and December, 1996. Dashed lines indicate one standard deviation. CIOM, RSM, and WSM indicate the central Indian Ocean maximum, Ross Sea maximum, and Weddell Sea maximum, respectively.

Figure 2. Daily ice edge anomaly in September and October as a function of longitudes.

Figure 3. Locations of ice-extent maxima in the central Indian Ocean, east of the Ross Sea, and in the Eastern Weddell Sea as a function of time during September and October, 1996.

Figure 4. Histograms of high westerlies ($U \geq 10ms^{-1}$) and high southerlies ($\mathrm{V} \geq 10\mathrm{ms}^{-1}$) along the sea ice edge (SIE) as a function of longitude for the ice maximum period. The mean SIE distribution in the same period is superimposed on the histograms.

Figure 5. (left column) Sea surface temperature and (right column) meridional gradient of the sea surface temperature at every degree of latitude north of the ice edge up to 5° of latitude for September, October, November, and December. Shaded areas indicate southerly winds north of the SIE in the monthly mean wind stress fields, while open areas indicate northerlies north of the SIE.

Figure 6. Schematic geostrophic winds (arrows) introduced by the sea ice distribution near the three ice-extent maxima. Solid line is the SIE in October 1996. Dashed line is the geopotential height anomaly 0.35 (10 J kg^{-1}) contour at 50 dB with respect to 1000 dB from *Orsi et al.* [1995]. Dotted lines are the positions of the ridges of standing wave number 3 from *van Loon and Jenne* [1972].

Figure 7. Mean propagation speed of sea ice maximum in the central Indian Ocean (circle), east of the Ross Sea (plus sign) and eastern Weddell Sea (asterisk) as a function of mean ice edge slope east of the ice maxima. Both the ice maximum propagation speed and ice edge slope are derived from monthly wind and sea ice data, and then averaged over September and October, 1996.

Plate 1. NASA scatterometer (NSCAT) wind stress magnitude from October 25 to October 30, 1996. A storm initiated in the marginal ice zone (MIZ) north of the Ross Sea ice maximum on October 25 and developed into a large storm event in the southeastern Pacific through October 30. Another storm started northeast of the Indian Ocean ice maximum on October 26 and spun off into the Antarctic Circumpolar Current region south of Australia through October 29.

Plate 2. NSCAT wind stress magnitude from October 7 to October 12, 1996. A storm started east of the Ross Sea ice maximum on October 7 and lasted 4 days. Another storm started northeast of the Weddell Sea ice maximum on October 8 and also lasted 3 days.

Plate 3. Spectral amplitude for (top) counterclockwise motions and (bottom) clockwise motions in the frequency

band of 5-10 days. Twice-daily wind stress data during the maximum ice period (47 days) are used to calculate the spectrum.

Plate 4. The mean NSCAT zonal wind stress τ_x, meridional wind stress τ_y and wind stress divergence for September and October, 1996. The September monthly mean is calculated from the available data between September 15 and September 31.

Plate 5. The monthly mean NSCAT τ_x, τ_y, and wind stress divergence for November and December, 1996.

Figure 1. The mean Antarctic sea ice edge (solid lines) derived from Special Sensor Microwave Imager ice concentration data for September, October, November, and December, 1996. Dashed lines indicate one standard deviation. CIOM, RSM, and WSM indicate the central Indian Ocean maximum, Ross Sea maximum, and Weddell Sea maximum, respectively.

Figure 2. Daily ice edge anomaly in September and October as a function of longitudes.

Figure 3. Locations of ice-extent maxima in the central Indian Ocean, east of the Ross Sea, and in the Eastern Weddell Sea as a function of time during September and October, 1996.

Figure 4. Histograms of high westerlies ($U \geq 10ms^{-1}$) and high southerlies ($\mathrm{V} \geq 10\mathrm{ms}^{-1}$) along the sea ice edge (SIE) as a function of longitude for the ice maximum period. The mean SIE distribution in the same period is superimposed on the histograms.

Figure 5. (left column) Sea surface temperature and (right column) meridional gradient of the sea surface temperature at every degree of latitude north of the ice edge up to 5° of latitude for September, October, November, and December. Shaded areas indicate southerly winds north of the SIE in the monthly mean wind stress fields, while open areas indicate northerlies north of the SIE.

Figure 6. Schematic geostrophic winds (arrows) introduced by the sea ice distribution near the three ice-extent maxima. Solid line is the SIE in October 1996. Dashed line is the geopotential height anomaly 0.35 (10 J kg^{-1}) contour at 50 dB with respect to 1000 dB from *Orsi et al.* [1995]. Dotted lines are the positions of the ridges of standing wave number 3 from *van Loon and Jenne* [1972].

Figure 7. Mean propagation speed of sea ice maximum in the central Indian Ocean (circle), east of the Ross Sea (plus sign) and eastern Weddell Sea (asterisk) as a function of mean ice edge slope east of the ice maxima. Both the ice maximum propagation speed and ice edge slope are derived from monthly wind and sea ice data, and then averaged over September and October, 1996.

Plate 1. NASA scatterometer (NSCAT) wind stress magnitude from October 25 to October 30, 1996. A storm initiated in the marginal ice zone (MIZ) north of the Ross Sea ice maximum on October 25 and developed into a large storm event in the southeastern Pacific through October 30. Another storm started northeast of the Indian Ocean ice maximum on October 26 and spun off into the Antarctic Circumpolar Current region south of Australia through October 29.

Plate 2. NSCAT wind stress magnitude from October 7 to October 12, 1996. A storm started east of the Ross Sea ice maximum on October 7 and lasted 4 days. Another storm started northeast of the Weddell Sea ice maximum on October 8 and also lasted 3 days.

Plate 3. Spectral amplitude for (top) counterclockwise motions and (bottom) clockwise motions in the frequency band of 5-10 days. Twice-daily wind stress data during the maximum ice period (47 days) are used to calculate the spectrum.

Plate 4. The mean NSCAT zonal wind stress τ_x, meridional wind stress τ_y and wind stress divergence for September and October, 1996. The September monthly mean is calculated from the available data between September 15 and September 31.

Plate 5. The monthly mean NSCAT τ_x, τ_y, and wind stress divergence for November and December, 1996.

Figure 1. The mean Antarctic sea ice edge (solid lines) derived from Special Sensor Microwave Imager ice concentration data for September, October, November, and December, 1996. Dashed lines indicate one standard deviation. CIOM, RSM, and WSM indicate the central Indian Ocean maximum, Ross Sea maximum, and Weddell Sea maximum, respectively.

Figure 2. Daily ice edge anomaly in September and October as a function of longitudes.

Figure 3. Locations of ice-extent maxima in the central Indian Ocean, east of the Ross Sea, and in the Eastern Weddell Sea as a function of time during September and October, 1996.

Figure 4. Histograms of high westerlies ($U \geq 10ms^{-1}$) and high southerlies ($\mathrm{V} \geq 10\mathrm{ms}^{-1}$) along the sea ice edge (SIE) as a function of longitude for the ice maximum period. The mean SIE distribution in the same period is superimposed on the histograms.

Figure 5. (left column) Sea surface temperature and (right column) meridional gradient of the sea surface temperature at every degree of latitude north of the ice edge up to 5° of latitude for September, October, November, and December. Shaded areas indicate southerly winds north of the SIE in the monthly mean wind stress fields, while open areas indicate northerlies north of the SIE.

Figure 6. Schematic geostrophic winds (arrows) introduced by the sea ice distribution near the three ice-extent maxima. Solid line is the SIE in October 1996. Dashed line is the geopotential height anomaly 0.35 (10 J kg^{-1}) contour at 50 dB with respect to 1000 dB from *Orsi et al*. [1995]. Dotted lines are the positions of the ridges of standing wave number 3 from *van Loon and Jenne* [1972].

Figure 7. Mean propagation speed of sea ice maximum in the central Indian Ocean (circle), east of the Ross Sea (plus sign) and eastern Weddell Sea (asterisk) as a function of mean ice edge slope east of the ice maxima. Both the ice maximum propagation speed and ice edge slope are derived from monthly wind and sea ice data, and then averaged over September and October, 1996.

Plate 1. NASA scatterometer (NSCAT) wind stress magnitude from October 25 to October 30, 1996. A storm initiated in the marginal ice zone (MIZ) north of the Ross Sea ice maximum on October 25 and developed into a large storm event in the southeastern Pacific through October 30. Another storm started northeast of the Indian Ocean ice maximum on October 26 and spun off into the Antarctic Circumpolar Current region south of Australia through October 29.

Plate 2. NSCAT wind stress magnitude from October 7 to October 12, 1996. A storm started east of the Ross Sea ice maximum on October 7 and lasted 4 days. Another storm started northeast of the Weddell Sea ice maximum on October 8 and also lasted 3 days.

Plate 3. Spectral amplitude for (top) counterclockwise motions and (bottom) clockwise motions in the frequency band of 5-10 days. Twice-daily wind stress data during the maximum ice period (47 days) are used to calculate the spectrum.

Plate 4. The mean NSCAT zonal wind stress τ_x, meridional wind stress τ_y and wind stress divergence for September and October, 1996. The September monthly mean is calculated from the available data between September 15 and September 31.

Plate 5. The monthly mean NSCAT τ_x, τ_y, and wind stress divergence for November and December, 1996.

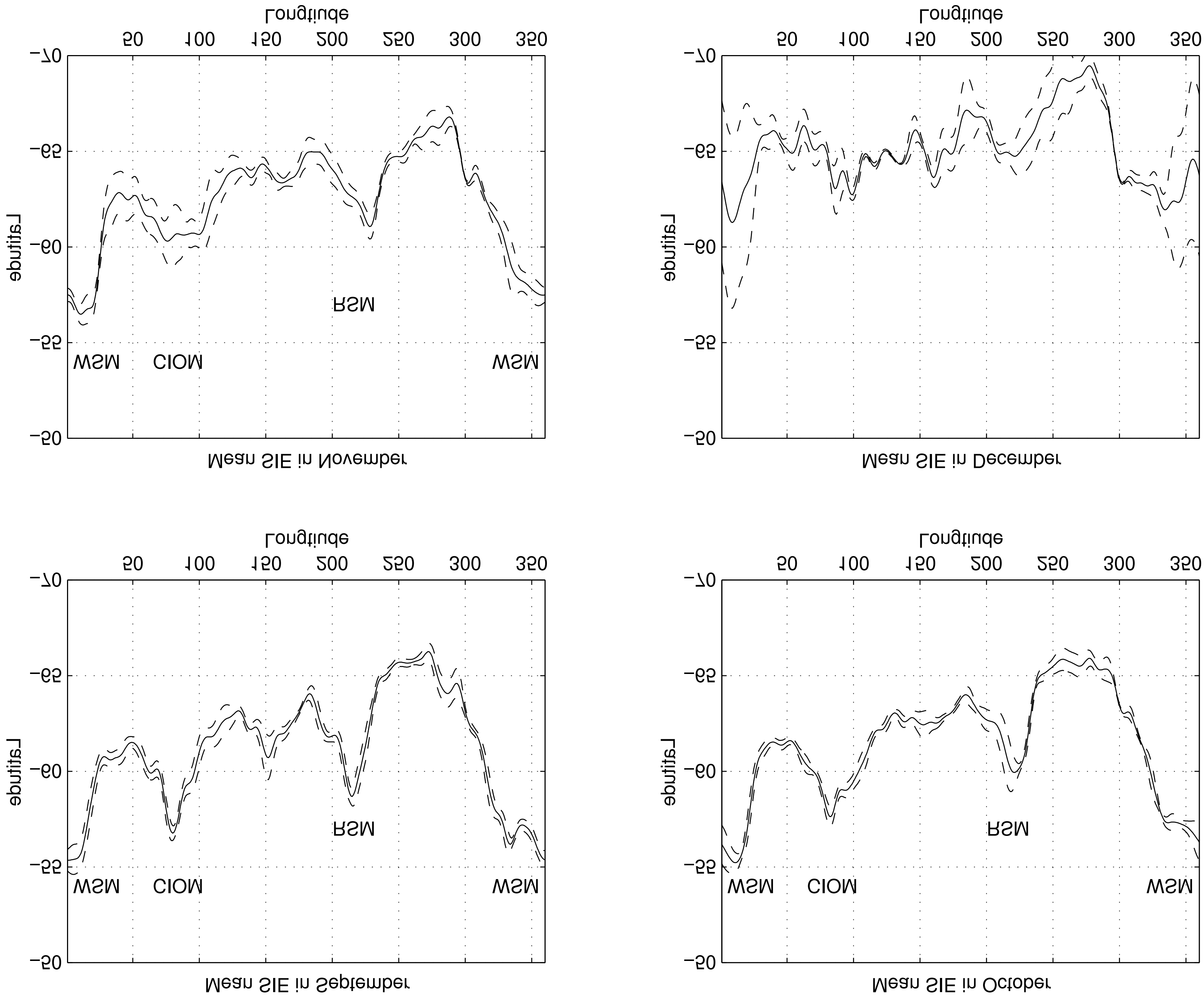
Mean SIE in September
Mean SIE in October
Mean SIE in November
Mean SIE in December
Longitude
Latitude
WSM
CIOM
RSM
50
100
150
200
250
300
350
−50
−55
−60
−65
−70

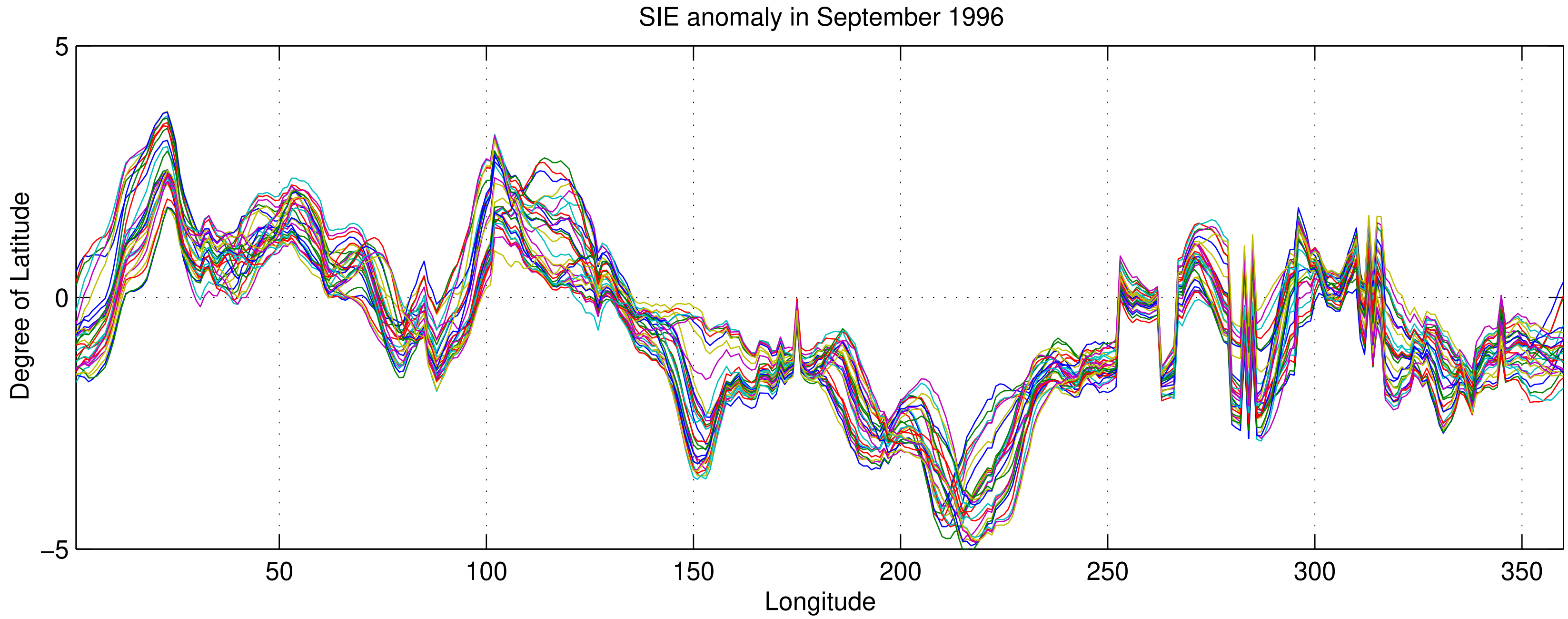
SIE anomaly in September 1996
Degree of Latitude
Longitude
5
0
−5
50
100
150
200
250
300
350

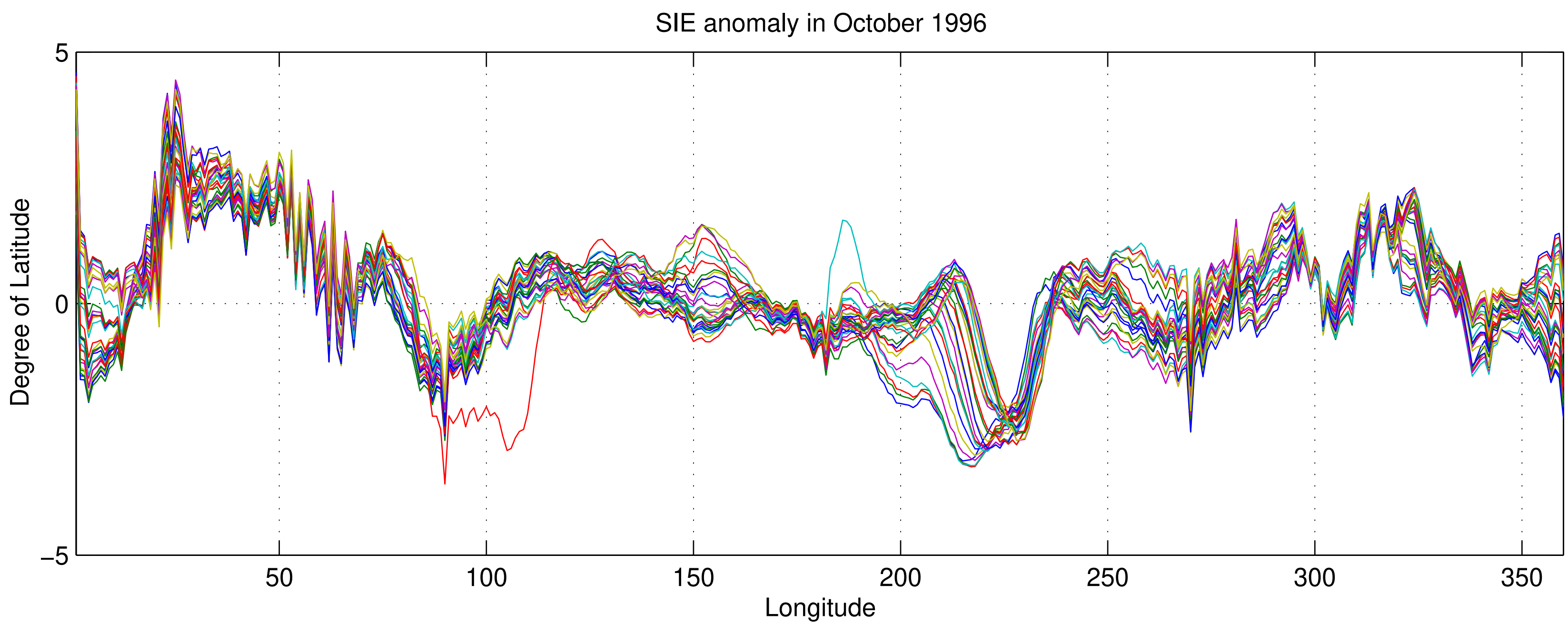
SIE anomaly in October 1996
Degree of Latitude
Longitude
5
0
−5
50
100
150
200
250
300
350

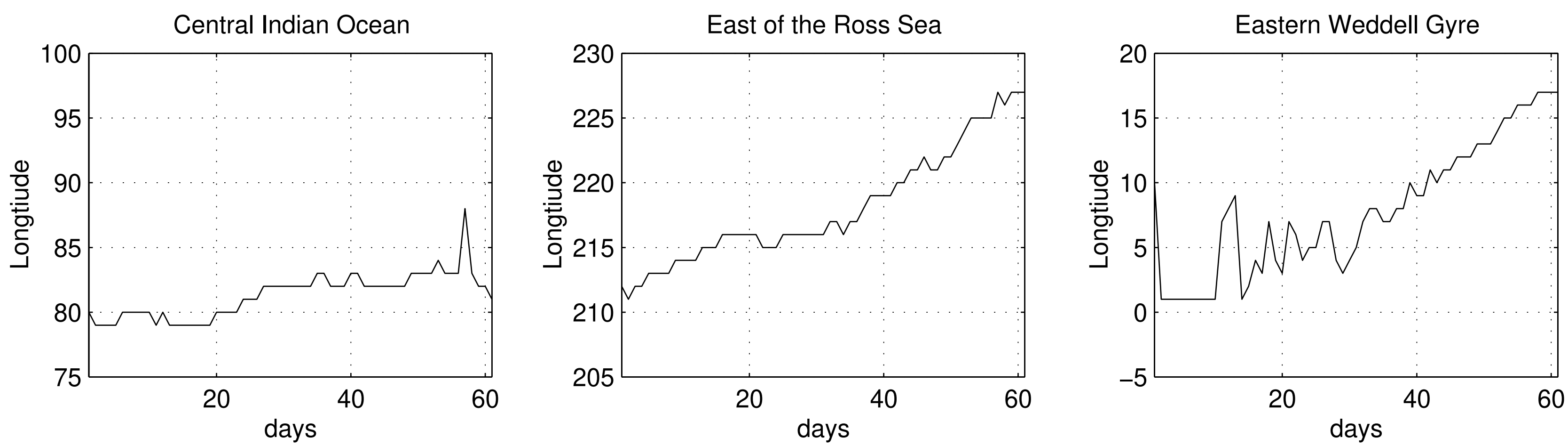

Central Indian Ocean
East of the Ross Sea
Eastern Weddell Gyre
Longtiude
days
100
95
90
85
80
75
230
225
220
215
210
205
20
15
10
5
0
−5
20
40
60

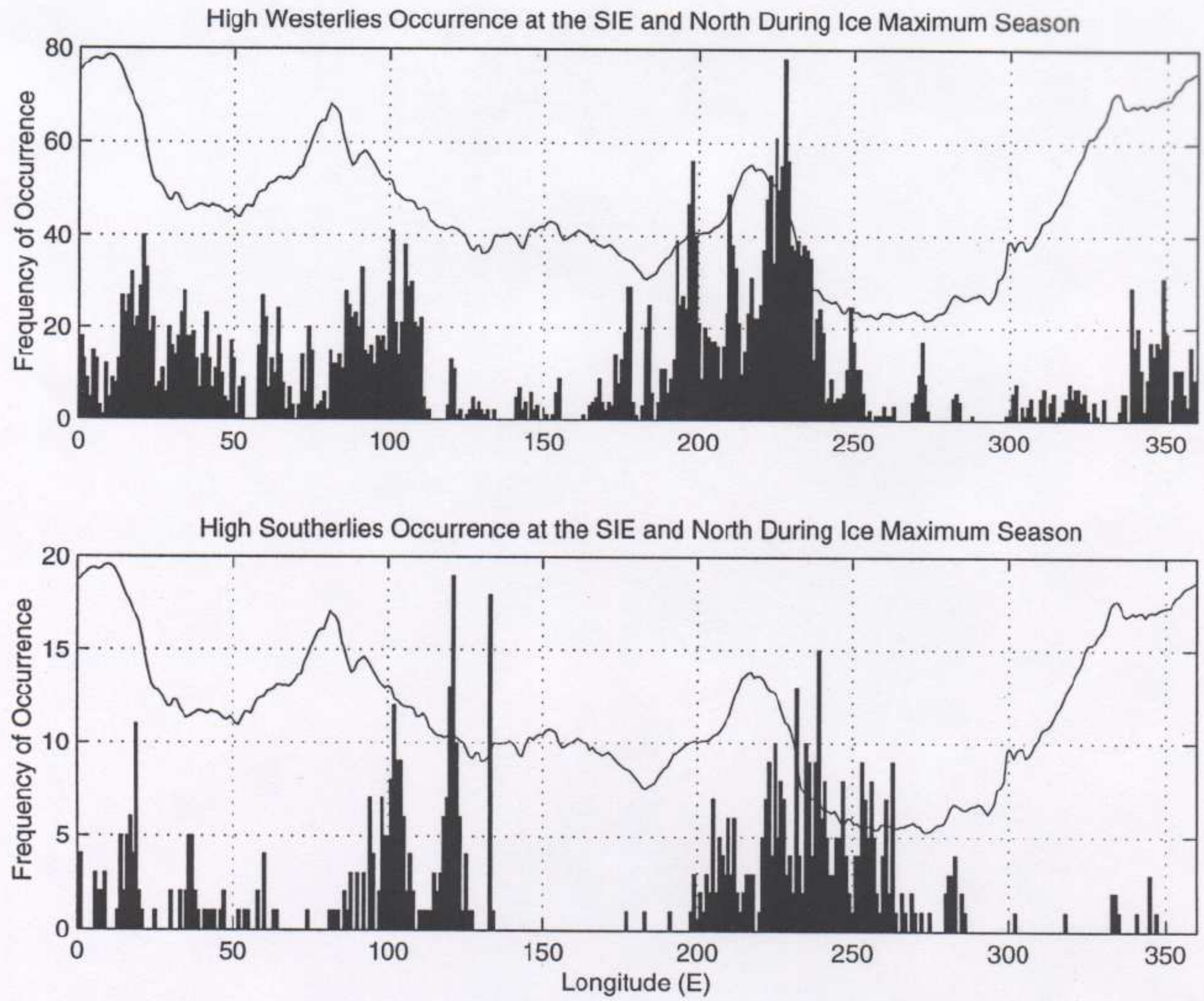

High Westerlies Occurrence at the SIE and North During Ice Maximum Season
Frequency of Occurrence
80
60
40
20
0
0
50
100
150
200
250
300
350
High Southerlies Occurrence at the SIE and North During Ice Maximum Season
Frequency of Occurrence
20
15
10
5
0
Longitude (E)

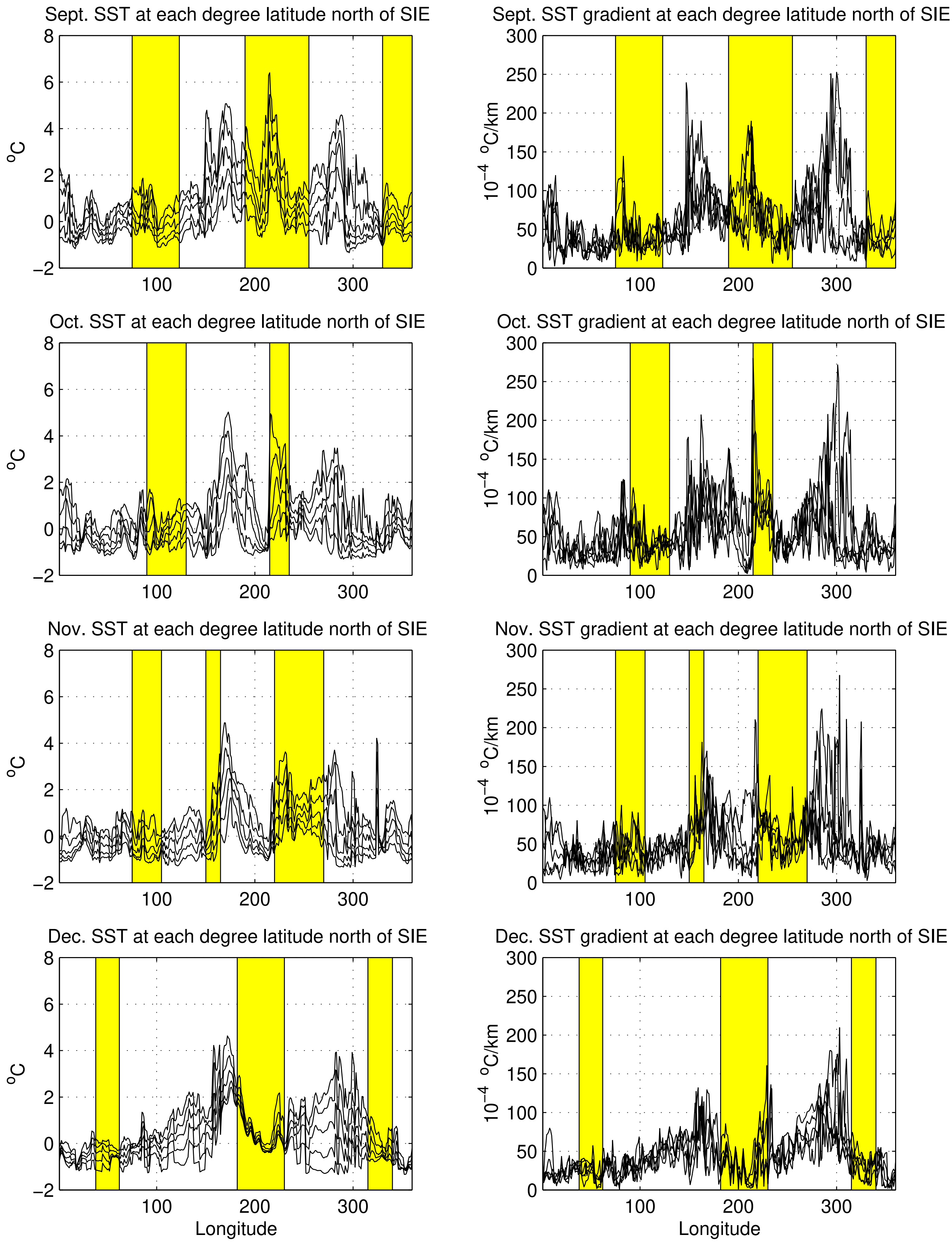

Sept. SST at each degree latitude north of SIE
Sept. SST gradient at each degree latitude north of SIE
Oct. SST at each degree latitude north of SIE
Oct. SST gradient at each degree latitude north of SIE
Nov. SST at each degree latitude north of SIE
Nov. SST gradient at each degree latitude north of SIE
Dec. SST at each degree latitude north of SIE
Dec. SST gradient at each degree latitude north of SIE
^oC
10^{-4} ^oC/km
Longitude

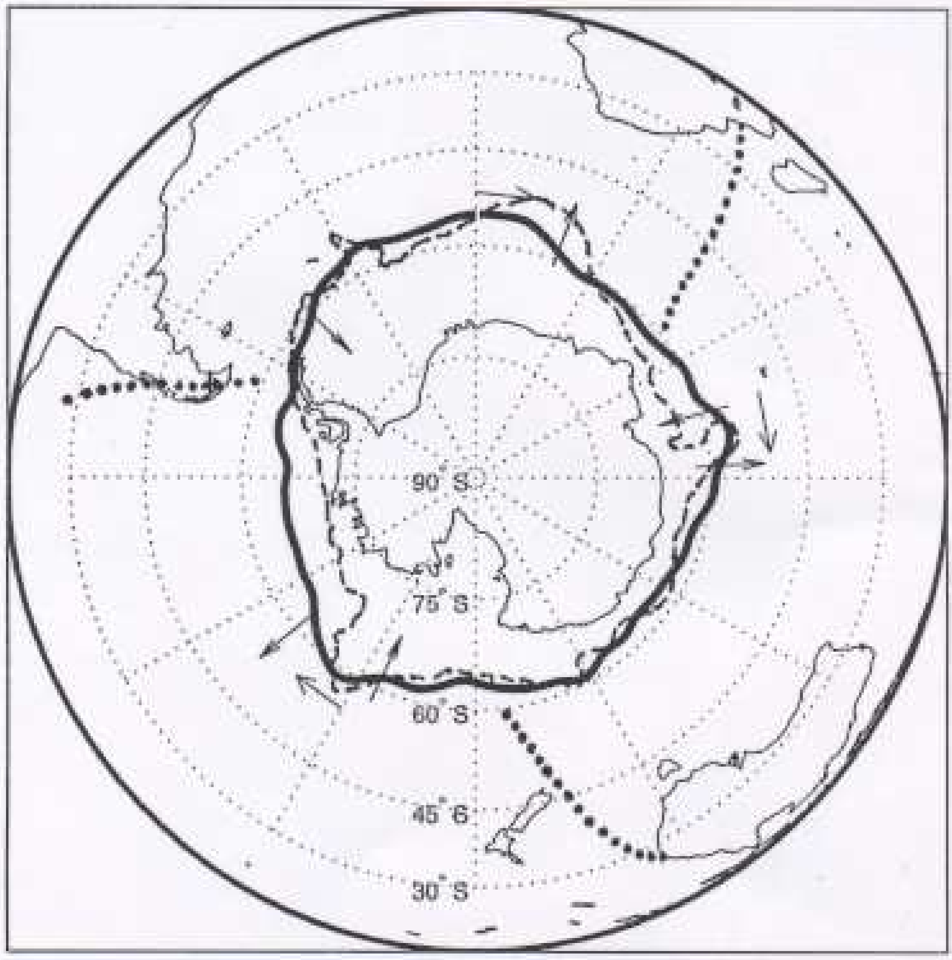

90° S
75° S
60° S
45° S
30° S

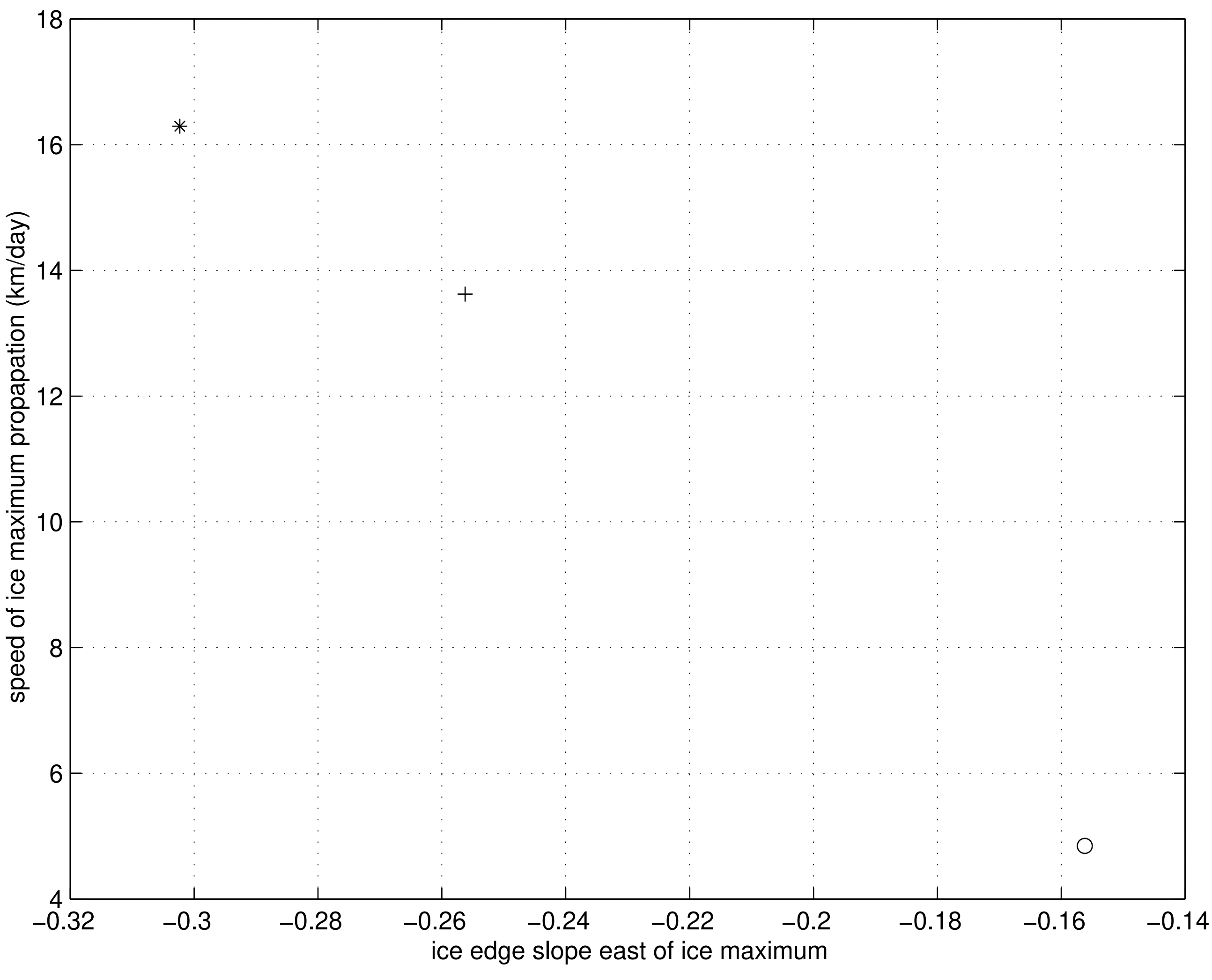

18
16
14
12
10
8
6
4
speed of ice maximum propapation (km/day)
−0.32
−0.3
−0.28
−0.26
−0.24
−0.22
−0.2
−0.18
−0.16
−0.14
ice edge slope east of ice maximum

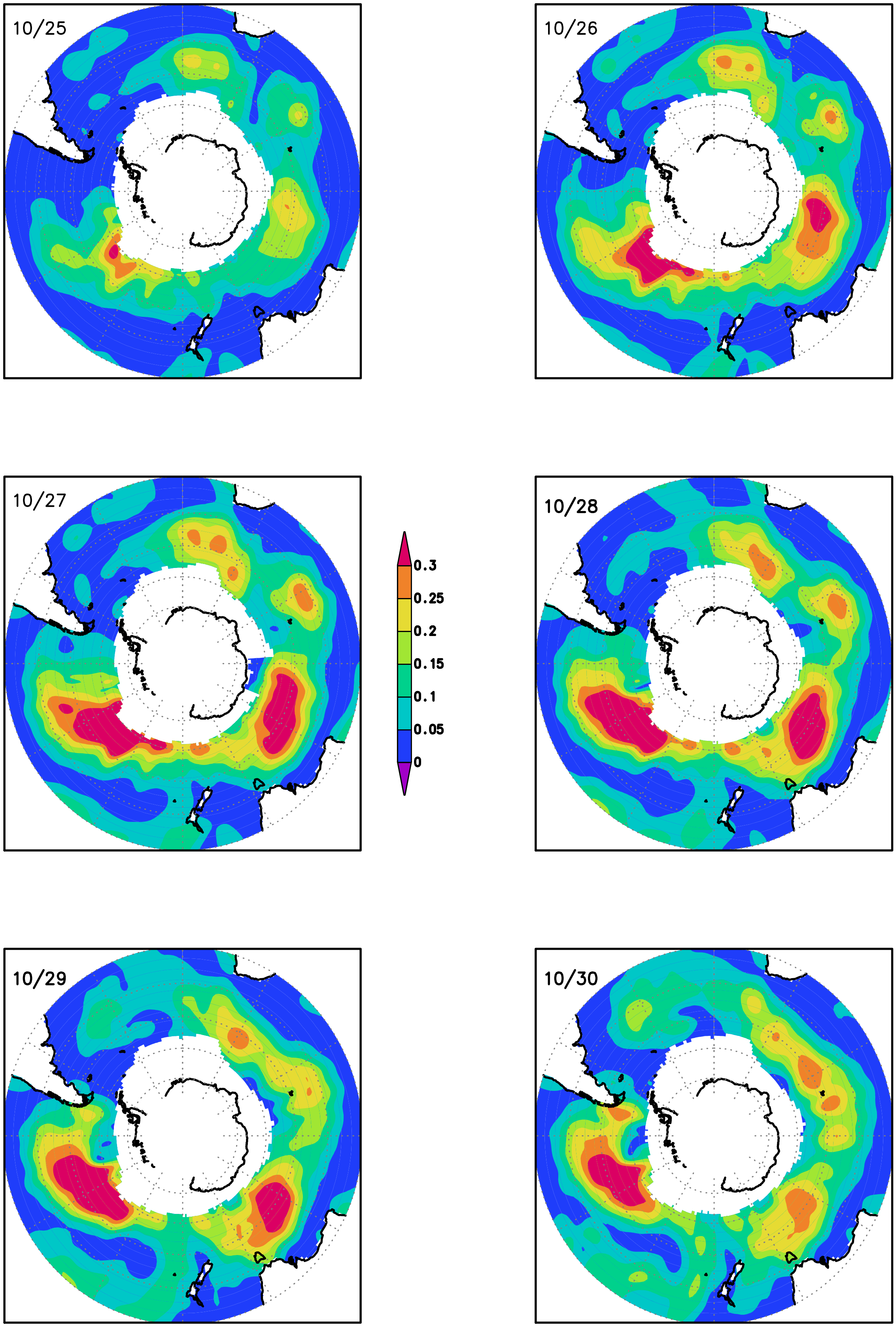
10/25
10/26
10/27
10/28
10/29
10/30
0.3
0.25
0.2
0.15
0.1
0.05
0

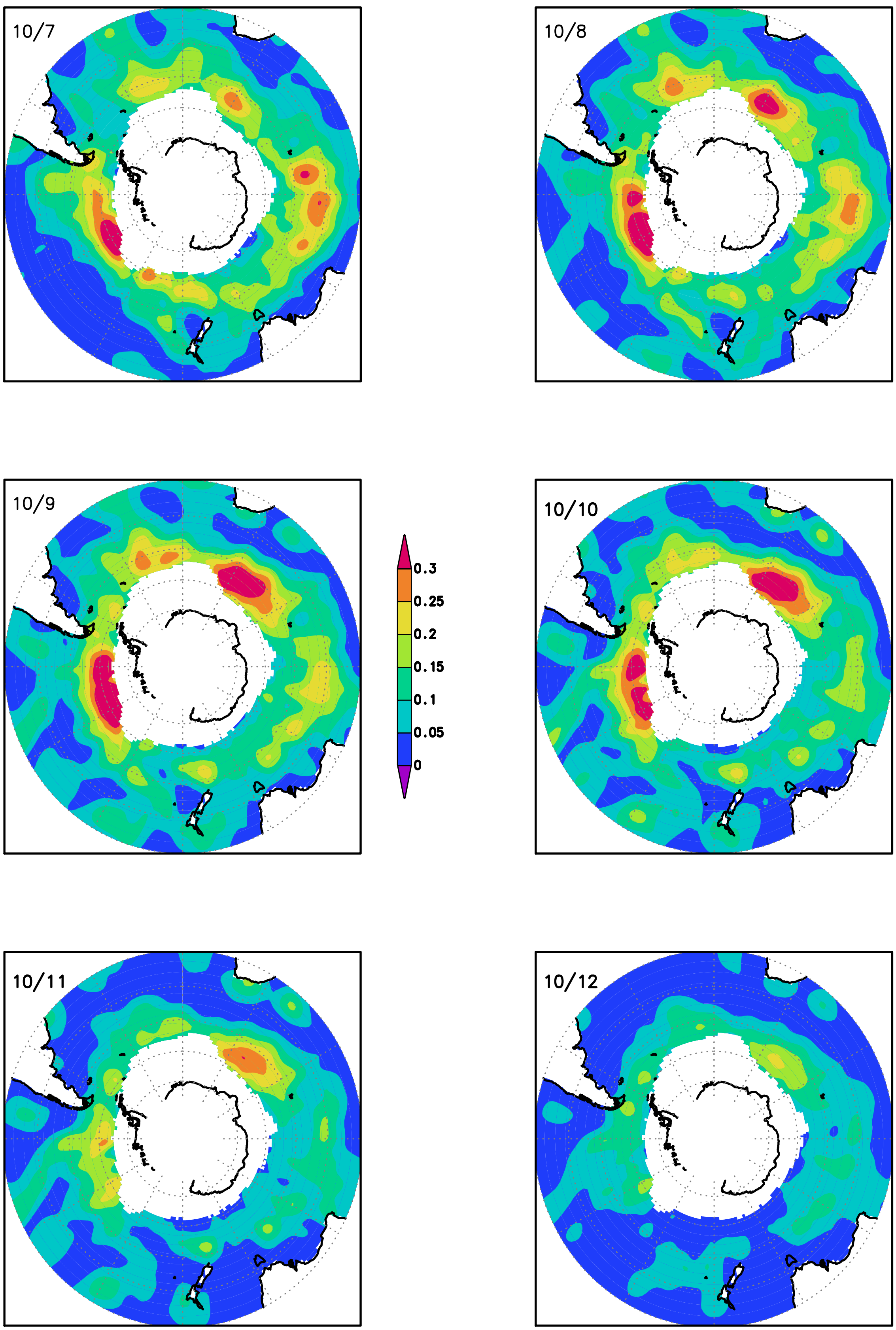
10/7
10/8
10/9
10/10
10/11
10/12
0.3
0.25
0.2
0.15
0.1
0.05
0

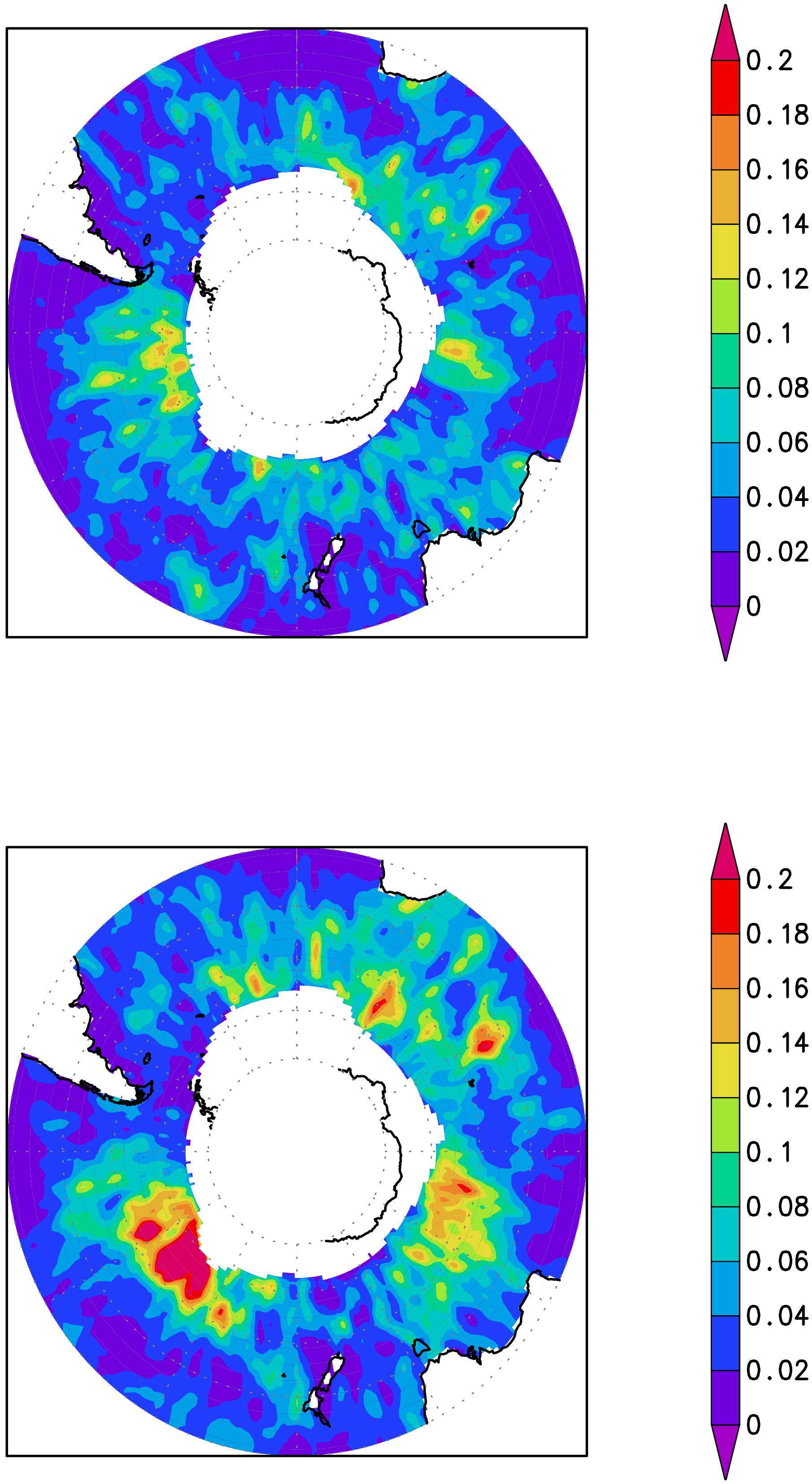
0.2
0.18
0.16
0.14
0.12
0.1
0.08
0.06
0.04
0.02
0
0.2
0.18
0.16
0.14
0.12
0.1
0.08
0.06
0.04
0.02
0

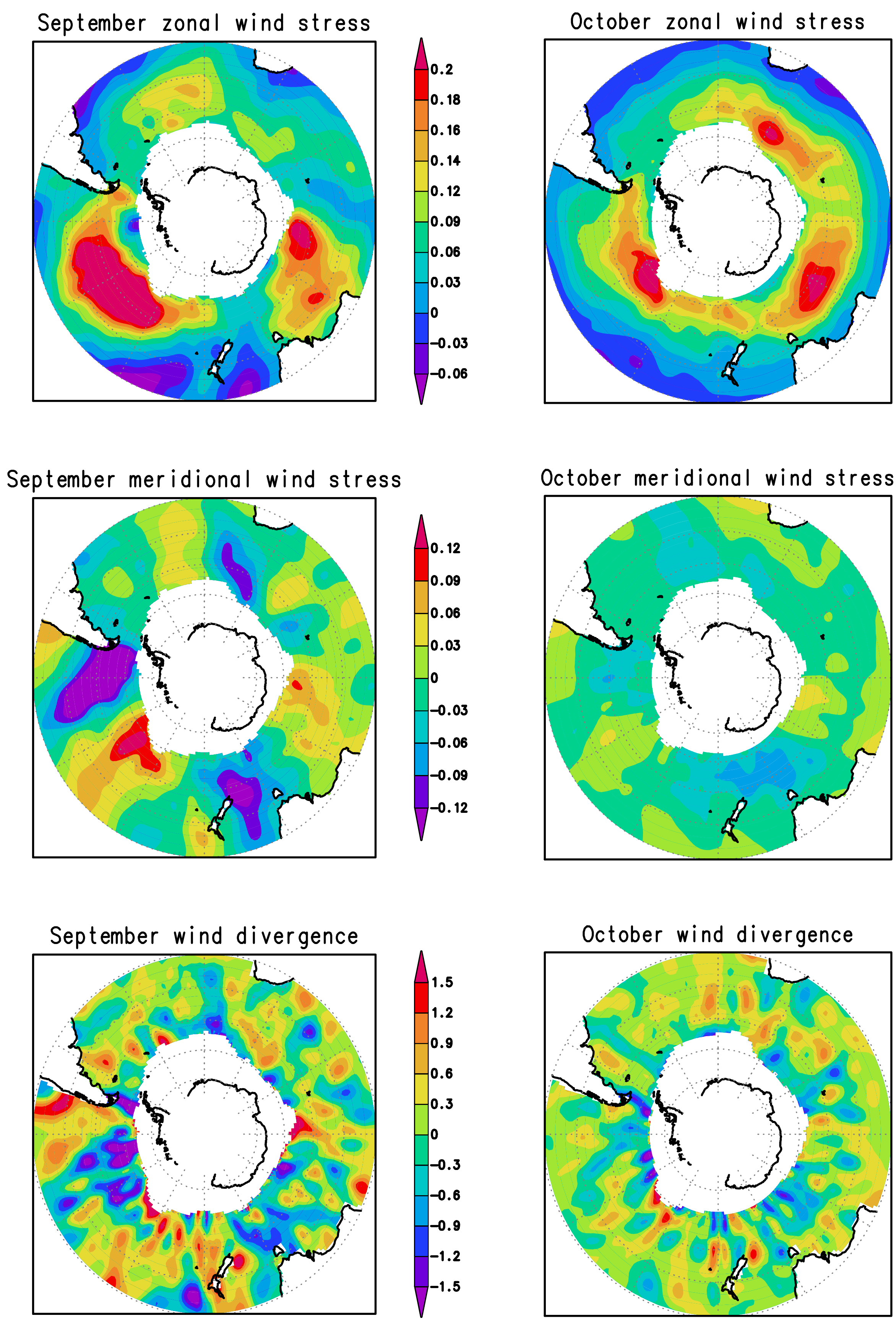
September zonal wind stress
October zonal wind stress
0.2
0.18
0.16
0.14
0.12
0.09
0.06
0.03
0
-0.03
-0.06
September meridional wind stress
October meridional wind stress
0.12
0.09
0.06
0.03
0
-0.03
-0.06
-0.09
-0.12
September wind divergence
October wind divergence
1.5
1.2
0.9
0.6
0.3
0
-0.3
-0.6
-0.9
-1.2
-1.5

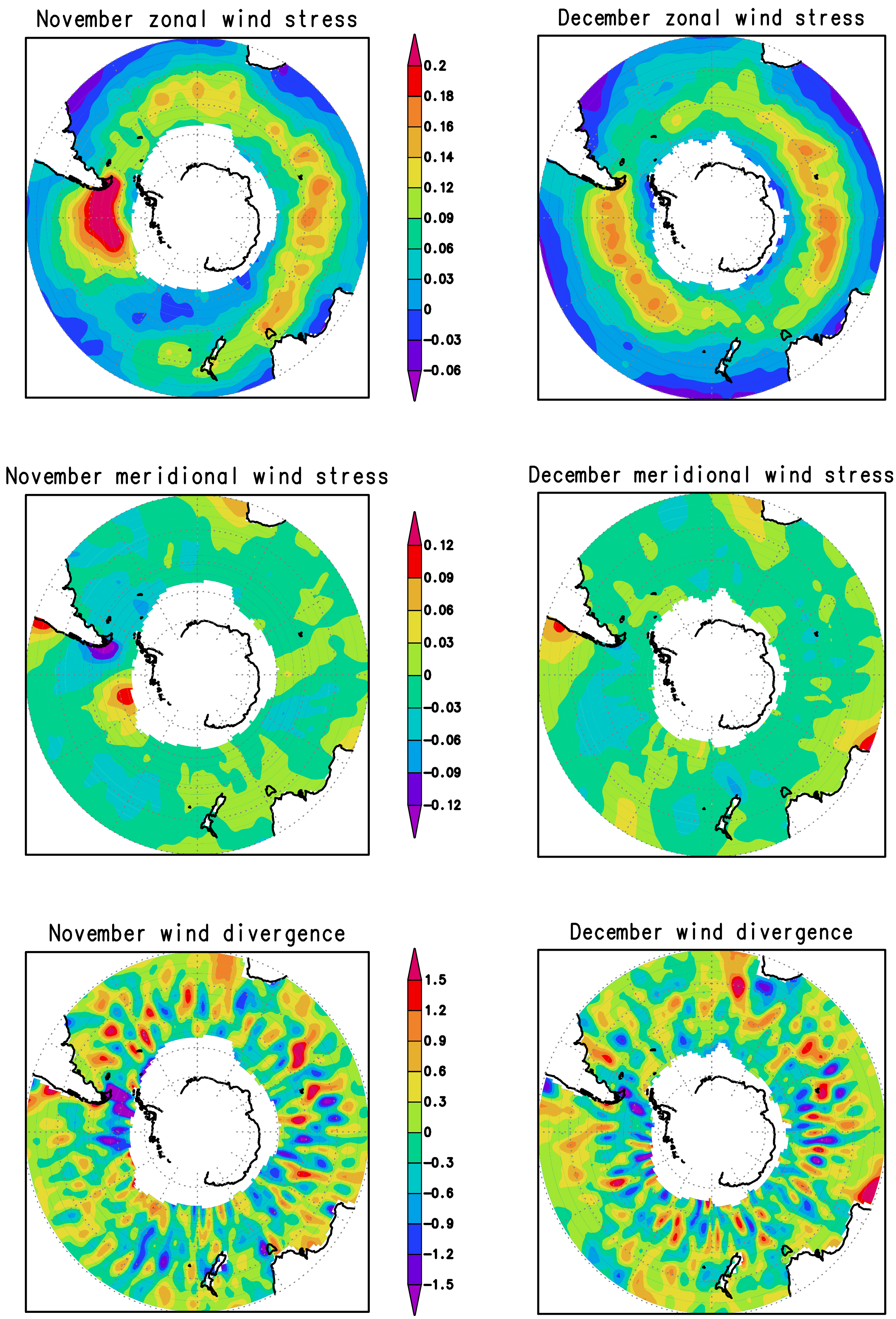
November zonal wind stress
December zonal wind stress
0.2
0.18
0.16
0.14
0.12
0.09
0.06
0.03
0
-0.03
-0.06
November meridional wind stress
December meridional wind stress
0.12
0.09
0.06
0.03
0
-0.03
-0.06
-0.09
-0.12
November wind divergence
December wind divergence
1.5
1.2
0.9
0.6
0.3
0
-0.3
-0.6
-0.9
-1.2
-1.5